Molecular Structure and Thermodynamics of CO_2 and Water Adsorption on Mica

Mert Aybar

Thesis submitted to the faculty of the Virginia Polytechnic Institute and State University in partial fulfillment of the requirements for the degree of

Master of Science
In
Mechanical Engineering

Rui Qiao, Chair

Jonathan B Boreyko

Xianming Bai

December 12th, 2025

Blacksburg, VA

Keywords: liquid-vapor interface, interfacial phenomena, adsorption, clay

Molecular Structure and Thermodynamics of CO_2 and Water Adsorption on Mica

Mert Aybar

ABSTRACT

The adsorption of CO_2 and water on clay surfaces plays a key role in applications such as gas storage in saline aquifers and depleted hydrocarbon reservoirs but is not yet fully understood. Here, the adsorption of CO_2 and water vapor is studied using Grand Canonical Monte Carlo and molecular dynamics simulations. At a bulk pressure of 100 bar, pure CO_2 adsorbs strongly on mica and forms extensive layers next to it. CO_2 adsorption is lowered substantially if introducing water vapor above mica and is largely eliminated when the relative humidity (RH) approaches about 60%. When pure water vapor is introduced above a mica surface, a sub-nm thick liquid water film develops on it to form apparent liquid-solid and liquid-vapor interfaces simultaneously. Using the ITIM (Identification of the Truly Interfacial Molecules) analysis, how individual water layers develops in this film as RH increases is delineated. It was discovered that the water film is spatially heterogeneous, and the true liquid-vapor interface emerges only at an RH of 60-80%. Introducing 100-bar CO_2 into the water vapor above the mica surface modulates water adsorption nonlinearly: at RH = 0.01%, the water adsorption is reduced by ≈30%; as RH increases, the reduction is weakened, and eventually, enhancement of water adsorption by about 7% occurs at RH = 90%. These variations are attributed to the interplay of film thinning by high-pressure CO_2, competition of mica surface sites by CO_2 molecules, and the energetic and entropic stabilization of interfacial water by CO_2 molecules.

This work has important implications for subsurface energy and environmental technologies. For example, it indicates that, in depleted unconventional reservoirs, assuming a completely dry environment can grossly overestimate the CO_2 storage contributed by adsorption on mineral

surfaces. Furthermore, it suggests that the swelling of clay in very low relative humidity can be suppressed by the displacement of interstitial water by high-pressure CO_2, which can compromise the mechanical integrity of caprocks in underground hydrogen storage sites employing CO_2 as cushion gas. These implications warrant experimental studies in the future.

Molecular Structure and Thermodynamics of CO_2 and Water Adsorption on Mica

Mert Aybar

GENERAL AUDIENCE ABSTRACT

Understanding how carbon dioxide (CO_2) and water interact with underground clay surfaces is essential for improving technologies like carbon storage and the long-term storage of gases in depleted reservoirs. Even tiny amounts of water in these formations can create ultra-thin films on mineral surfaces, which in turn change how gases behave. Yet the details of these interactions remain difficult to observe directly. In this study, we use advanced computer simulations to explore how CO_2 and water compete for space on the surface of mica, a common clay mineral. We find that CO_2 alone forms dense layers on the surface under high pressure, but even small amounts of water vapor begin to push CO_2 away. As humidity rises, water eventually forms a thin, patchy liquid film that becomes more uniform only at higher moisture levels. This water film strongly limits how much CO_2 can attach to the surface. We also show that CO_2, under some conditions, changes how water behaves. At very low humidity, CO_2 reduces the amount of water that sticks to the surface, while at high humidity, it slightly increases water uptake. These changes result from a balance between CO_2 squeezing the water film, competing with water for surface sites, and stabilizing the structure of the water at the interface.

Acknowledgements

I would first like to express my deepest gratitude to my advisor, Prof. Rui Qiao, for his unwavering support throughout my graduate studies. His mentorship has shaped not only my development as a researcher but also as an effective communicator. I am sincerely grateful for the opportunities he provided, the trust he placed in me, and his willingness to encourage my pursuit of research topics aligned with my interests. His guidance has been invaluable to both my academic and personal growth.

I would also like to thank my committee members, Dr. Boreyko and Dr. Bai, for their continued support, insightful feedback, and guidance. Their support has greatly enriched this work.

I gratefully acknowledge the support of Virginia Tech’s Advanced Research Computing (ARC), whose computational resources made much of this research possible.

My sincere thanks go to the members of the Transport Phenomena Laboratory (TPL) for fostering a supportive, collaborative, and friendly research environment. I am especially indebted to Dr. Hongwei Zhang for helping me with molecular dynamics and for his generous help throughout my research. I would also like to thank Dr. Jacob Wilson, Paige Brockway, Ruiyang Ji, and my other lab mates for their continued encouragement and assistance.

Lastly, I thank my family, especially my parents, for their unconditional support and the countless sacrifices they have made on my behalf. Nothing I achieve would be possible without them, and I remain forever grateful.

Contents

List of Figures ix

Chapter 1. Introduction 1

1.1 CO_2 Sequestration and the Role of Water–CO_2 Interactions in Geological Storage 1

1.2 Underground Hydrogen Storage and the Role of CO_2–H_2O Interactions 3

Chapter 2. Literature Review 6

Chapter 3. Simulation Systems, Models, and Methods 10

3.1 Molecular Systems 10

3.2 Molecular Models 11

3.3 Simulation Methods 11

3.4 Interfacial Structure Analysis 12

Chapter 4. Results and Discussion 15

4.1 Adsorption of Pure CO_2 and Water on Mica Surfaces 15

4.1.1 Pure CO_2 15

4.1.2 Pure Water 16

4.2 Co-adsorption of CO_2 and Water on Mica Surfaces 20

4.2.1 Qualitative Features 20

4.2.2 Quantitative aspects of CO_2 adsorption 22

4.2.3 Quantitative aspects of water adsorption 26

Chapter 5. Conclusions 30

References 32

Appendices 37

Appendix I - Method for computing the interaction energies shown in Fig. 12c and 13 37

Appendix II - Density, orientation and dynamics of water molecules near mica surfaces 38

Appendix III - Selection of representative position for water molecules directly exposed to vapor 41

Appendix IV - Interaction energy of water molecules near the water-vapor interface 42

List of Figures

Fig. 1. Trend of CO_2 concentration in the atmosphere.[4] The figure is taken from Ref. 4 with permission from KeAi Publishing. 2

Fig. 2. (**a**) CO_2-brine-rock interaction during sequestration with black arrow indicating the direction of CO_2 flow.[2] The figure is taken from Ref. 2 with permission from MDPI. (**b**) Types of trapping mechanisms and their timescales.[1] The figure is taken from Ref. 1 with permission from Elsevier. 3

Fig. 3. Types of utilization of hydrogen as a clean fuel.[9] The figure is taken from Ref. 9 with permission from Yandy Scientific Press. 4

Fig. 4. (**a**) Types of Geological storage of hydrogen with their respective storage power and discharge time. Ranges for each type indicate variations in storage site size and operational management.[8] The figure is taken from Ref. 8 with permission from GeoScienceWorld. (**b**) Schematic of an aquifer structure before (left) and after (right) hydrogen storage.[9] The figure is taken from Ref. 9 with permission from Yandy Scientific Press. 5

Fig. 5. Snapshots of molecular systems for studying adsorption of pure CO_2 (**a**), pure water (**b**), and CO_2 + water vapor mixture on mica (**c**). The origin of the z axis ($z = 0$) corresponds to the surface oxygen plane of the lower mica wall. In (c), to better delineate to what extent CO_2 molecules can approach mica (in particular, its surface K atoms), the water molecules within 0.6 nm of the lower mica surface are not shown. Water and CO_2 molecules are shown using blue and red ball-and-stick models. In mica, the K atoms are shown as yellow balls, and all other atoms are shown as grey balls. 10

Fig. 6. A schematic for the determination of individual molecular layers adsorbed on a solid surface using the ITIM (Identification of the Truly Interfacial Molecules) methodology. 14

Fig. 7. Density profile of CO_2 near the lower mica wall when the CO_2 pressure is 100 bar. The vertical dashed line marks the position of surface K^+ ions. The inset is the distribution of the CO_2-mica interaction energy for CO_2 molecules in the first density peak. A CO_2 molecule's position is computed based on its carbon atom. 15

Fig. 8. (**a**) Density profiles of pure water near the lower mica wall when the relative humidity (RH) in the mica channel is varied. Water molecules' positions are computed based on their oxygen atoms. (**b**) The adsorption isotherms of water on mica in the absence and presence of a 100 bar CO_2 atmosphere. In (a), 1, 2, 3, and 4 mark the four main density peaks. Water density profiles in (a) are also shown in separate panels for different RHs in Fig. S1 Appendix II. 16

Fig. 9. (**a-h**) Representative snapshots of individual water layers atop mica surfaces with RH of 0.01% to 90% in the top view. The first layer, in contact with the mica wall, is colored blue. The second (third) water layer, positioned above the first (second) layer, is colored green (magenta). The surface K^+ ions are colored yellow. 18

Fig. 10. The evolution of the areal density of the first, second, and third water layers atop the mica surface as a function of the environmental RH. 19

Fig. 11. Density profiles of CO_2 and water near the lower mica wall when the CO_2 environmental pressure is kept at 100 bar while RH is varied from 0.01% to 90%. Density profiles are also shown in separate panels for different RHs in Fig. S1 Appendix II. 21

Fig. 12. (**a**) CO_2 adsorption isotherm as a function of the RH. (**b**) A comparison of the CO_2 density profile near the lower mica wall when the RH is 0 and 0.01%. (**c**) Distribution of the interaction energy of adsorbed CO_2 (pCO2 = 100 bar, RH = 0) and water (pCO2 = 0; RH = 0.01%) molecules with the mica wall. 22

Fig. 13. Distribution of the interaction energy of contact adsorbed CO_2 molecule ($z < 0.32$ nm) with mica and water at RH of 0.01% and 1%. (a) CO_2-water interactions. (b) CO_2-mica interactions. 23

Fig. 14. Density distribution of water molecules around CO_2 molecules positioned at 0.4 nm above the mica surface at RH of 0.01% to 90%. The density is plotted as a function of the water molecules' *z*-position (Z) and their distance from the CO_2 molecule's C atom (cf. the filled white semicircle) in the *xy*-plane (i.e., the lateral direction, R). The CO_2 environmental pressure is 100 bar. 25

Fig. 15. (**a**) The orientation distribution of the OH bond of water molecules located at the position where the water density is 5.65 nm^{-3} (cf. the filled black circles in Fig. 10). Solid (dashed) lines are for situations with CO_2 pressure of 100 bar (0 bar). (**b**) The average interaction energy of water molecules located at the position where the water density is 5.65 nm^{-3}. 29

Fig. S1. Comparison of the water density profiles near the lower mica wall when the environmental CO_2 pressure is 0 bar and 100 bar at different RHs. 38

Fig. S2. Orientation distribution of the OH bond of water molecules in the regions $0 < z < 0.22$ nm (i.e., the first water peak at RH = 0.01%) and 0.22 nm $< z <$ 0.32 nm. 38

Fig. S3. A comparison of the continuous survival probability function (a) and the dipole orientational autocorrelation function (b) for water molecules in the first density peak near the mica surface obtained in this study and by Malani and Ayappa.[48] In Malania and Ayappa's work, water is confined between two mica sheets. In our data shown here, the RH of the water vapor above the mica is 0.01%. 40

Fig. S4. The probability density distribution of the *z*-position of molecules in the three interfacial water layers on a mica surface at RH = 90%. To compute these distributions, for each saved trajectory frame, we first identify molecules belonging to the first, second, and third interfacial layers as discussed in the main text. Then, for water molecules in each of these layers, we build a histogram based on their oxygen atoms' z-position, from which the probability density distribution is computed. 41

Fig. S5. The average interaction energy of water molecules located at the position where the water density is 5.65 nm^{-3}. Solid (dashed) lines are for situations with a CO_2 pressure of 0 bar (100 bar). 42

Chapter 1. Introduction

The adsorption of CO_2 and water on minerals under unsaturated conditions plays a fundamental role in controlling the subsurface behavior of fluids. These interfacial processes influence how gases partition between solid and fluid phases, how wetting characteristics evolve, and how minerals react. Consequently, these processes underpin many geological and engineering applications, from carbon sequestration to underground hydrogen storage.[1–12] In carbon storage systems, the interaction between CO_2, water, and mineral surfaces governs the efficiency of solubility trapping and affects long-term containment.[1–7] On the other hand, in hydrogen storage formations, where residual water films and caprock-bound brines are ubiquitous, similar interfacial phenomena dictate gas mobility, cyclic recovery, and pressure stability during injection and withdrawal.[8-11]

1.1 CO_2 Sequestration and the Role of Water–CO_2 Interactions in Geological Storage

Atmospheric CO_2 levels has been continually increasing over the past decades as a direct consequence of burning of fossil fuels (see Fig. 1).[1] Carbon capture, utilization, and storage (CCUS) methods have become an important approach to mitigate the presence of greenhouse gases with geological sequestration emerging as a viable method.[2] In CCUS, CO_2 is often injected into deep underground formations such as depleted oil and gas fields, unmineable coal seams, and deep saline aquifers.[1,3] Owing to their vast global distribution and high storage capacity estimated up to 10^4 gigatons of CO_2, corresponding to centuries of projected emissions, saline aquifers are especially promising for formation selection.[1]

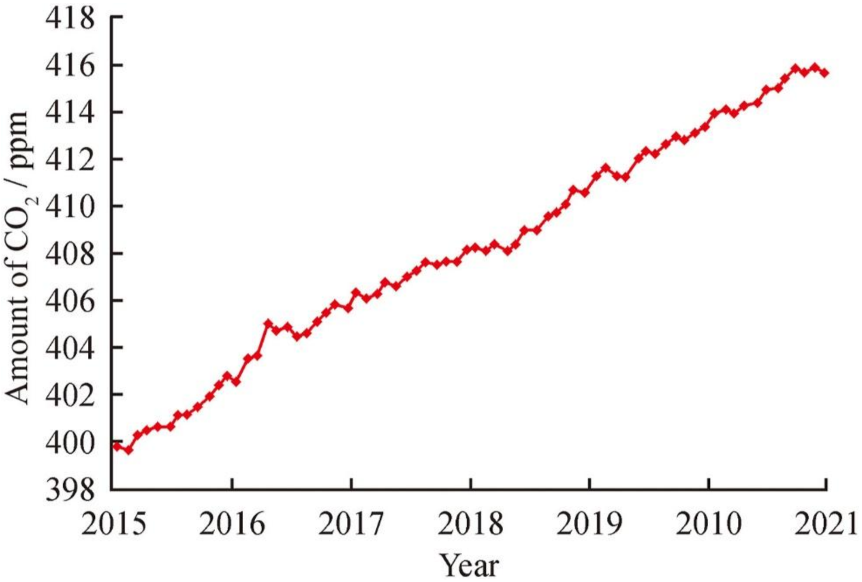

Fig. 1. Trend of CO_2 concentration in the atmosphere.[4] The figure is taken from Ref. 4 with permission from KeAi Publishing.

In saline formations, CO_2 is immobilized through several trapping mechanisms, primarily geological, hydrodynamic, and geochemical.[1] Geological trapping occurs beneath impermeable caprocks, hydrodynamic trapping through capillary forces, and geochemical trapping via dissolution of CO_2 into brine and mineralization into stable carbonates (see Fig. 2a). The success of storage depends on selecting formations with low seismic activity, limited fracturing, and adequate porosity–permeability to ensure injectivity and long-term containment.[4] Once injected, the buoyant CO_2 plume migrates upward, contacting brine and caprock surfaces, where CO_2–water–rock interactions control both the chemical and mechanical evolution of the reservoir (see Fig. 2b).[2]

The presence of water plays a defining role in CO_2 storage efficiency. In clay-rich formations such as muscovite, CO_2 can adsorb physically within micropores and interlayers, providing additional storage capacity.[5] However, as humidity and water content increase, CO_2 adsorption capacity decreases sharply, since water occupies sorption sites and swells clay interlayers. This competition limits physical adsorption while promoting solubility and mineral trapping, which can enhance long-term stabilization.

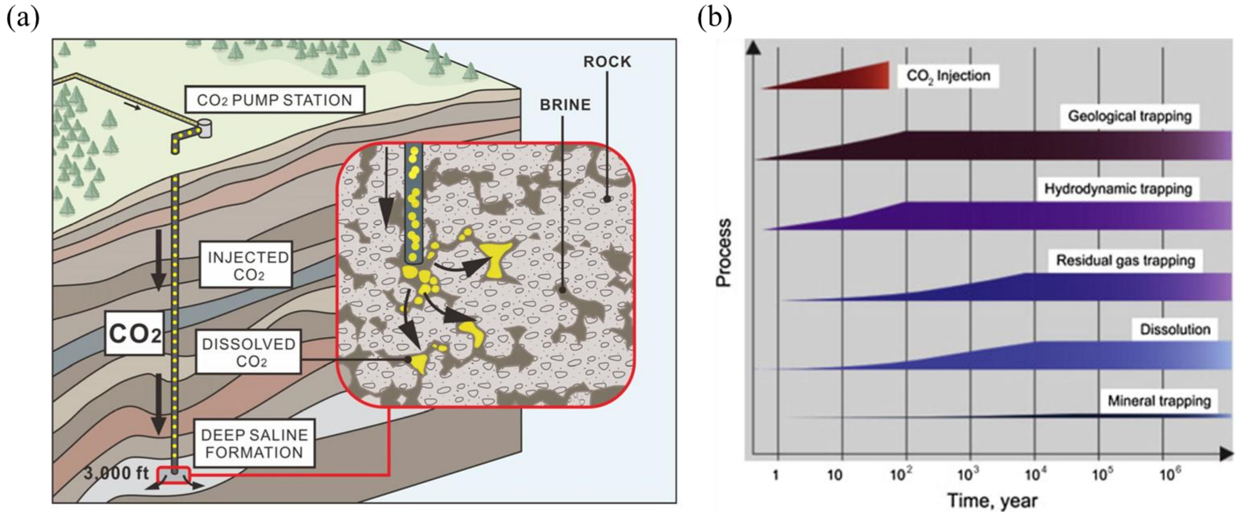

Fig. 2. (**a**) CO_2-brine-rock interaction during sequestration with black arrow indicating the direction of CO_2 flow.[2] The figure is taken from Ref. 2 with permission from MDPI. (**b**) Types of trapping mechanisms and their timescales.[1] The figure is taken from Ref. 1 with permission from Elsevier.

1.2 Underground Hydrogen Storage and the Role of CO_2–H_2O Interactions

While global fossil fuel remains the leading energy resource with its use accounting for around 80% of energy consumption and is expected to decline only slightly to 73% by 2030, employment of hydrogen offers an alternative towards mitigating effects of greenhouse gases.[8,9] In regard to decarbonizing energy systems, providing a clean solution to the intermittency of renewable energy sources such as solar, wind, and hydroelectric power; hydrogen has emerged as an important utility (see Fig. 3).

Highly fluctuating nature of renewable energy generation makes long-term energy storage essential to balance supply and demand. Hydrogen's high gravimetric energy density (120 kJ g^{-1}) makes it a promising carrier for seasonal-scale energy storage, with underground hydrogen storage (UHS) capable of reaching capacities from 100 GWh up to 1 EJ (10^{18} J) roughly equivalent to 0.2% of the annual consumption (2021).[10]

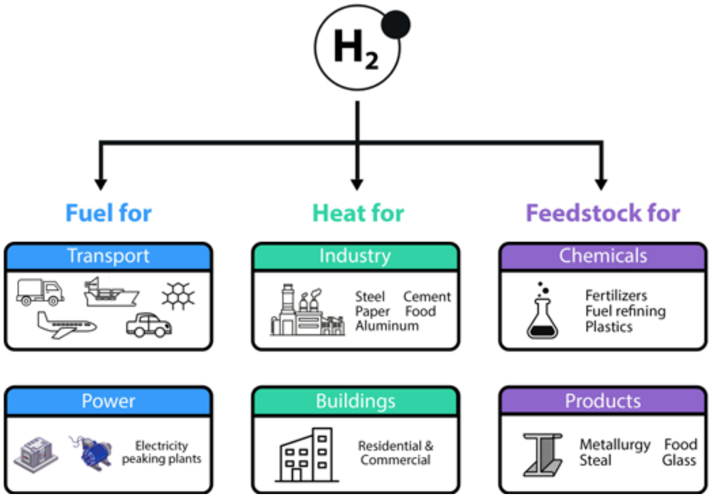

Fig. 3. Types of utilization of hydrogen as a clean fuel.[9] The figure is taken from Ref. 9 with permission from Yandy Scientific Press.

Geological formations can provide viable environment for large-scale, long-duration hydrogen storage in both capacity and containment. The main formation types under consideration are depleted hydrocarbon reservoirs, aquifers, salt caverns, and hard rock caverns. Storage is contingent upon the type of geology, depth, pressure, capacity cap rock, reservoir permeability, and porosity of these formations (see Fig. 4a).[10] Stemming from the cyclic nature of the process, choice and usage of cushion gasses are pivotal for stabilizing the reservoir, maintaining pressure and preventing gas trapping.[8-10] Amongst possible options, CO_2 offers a dual advantage when used as it contributes to carbon sequestration while being used as a cushion gas.

In geological reservoirs, water is inherently present in the pore spaces and at mineral interfaces, making the interaction between CO_2 and H_2O a critical factor in determining storage stability and performance (see Fig. 4b). [8-10] The coadsorption and interactions between CO_2 and H_2O at mineral interfaces dictate how gas molecules partition between the aqueous and gaseous phases; affecting hydrogen's mobility, recovery efficiency, and leakage risk during storage cycles.[8] Additionally, molecular dynamics (MD) simulations have shown hydrogen diffusion in water-saturated clay minerals to be significantly influenced by the type of exchangeable cations and the distribution of layer charges.[9]

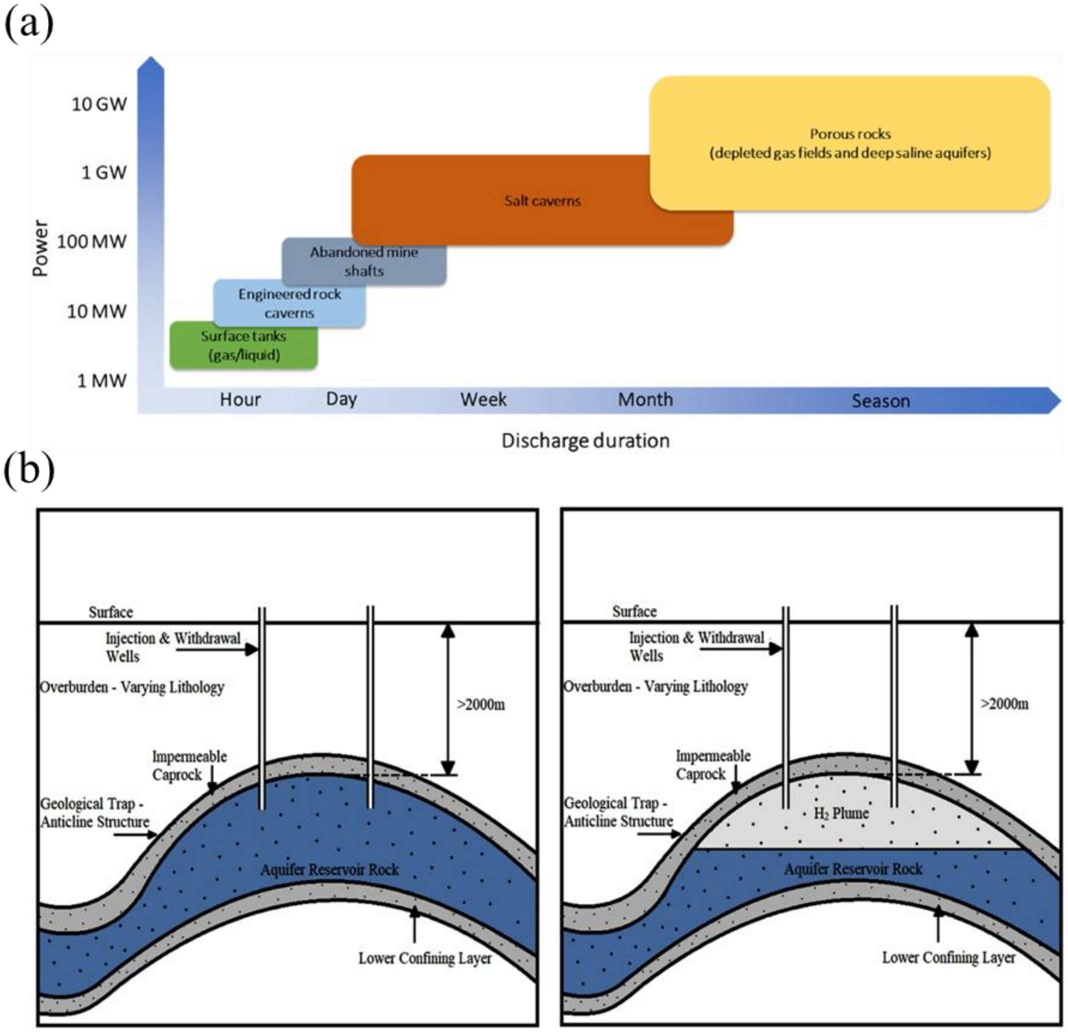

Fig. 4. (**a**) Types of Geological storage of hydrogen with their respective storage power and discharge time. Ranges for each type indicate variations in storage site size and operational management.[8] The figure is taken from Ref. 8 with permission from GeoScienceWorld. (**b**) Schematic of an aquifer structure before (left) and after (right) hydrogen storage.[9] The figure is taken from Ref. 9 with permission from Yandy Scientific Press.

Chapter 2. Literature Review

Because of the technical applications described in Chapter 1 and in other engineering areas, the adsorption of CO_2 and water on mineral surfaces has been investigated through a wide range of experimental and computational techniques. Molecular-scale simulations, especially Grand Canonical Monte Carlo (GCMC) and MD, have become central tools as they enable direct access to adsorption behavior at atomistic scale. GCMC is particularly valuable for predicting adsorption isotherms thus, offering insights that are often difficult or impossible to obtain experimentally due to the complexity of subsurface systems. Similarly, MD enables the examination of structural organization and dynamical processes that govern mineral–fluid interactions. These approaches have been widely applied to study water uptake in clay minerals and the competitive adsorption of gases in shale, where experimental observation of adsorption mechanisms is challenging.[13-17]

For CO_2, simulations revealed that it can adsorb strongly on the surface of minerals and surface saturation can occur at low bulk CO_2 densities.[18-24] Zhang et al.[25] showed through molecular simulations that CO_2 preferentially adsorbs on mineral surfaces such as calcite, quartz, and montmorillonite, often achieving surface saturation at relatively low bulk conditions and exhibiting a strong ability to displace both light and heavy hydrocarbons. Building on this understanding, they examined CO_2–C8 mixtures in calcite nanopores and found that CO_2 forms a stable adsorbed layer on the pore surface and can displace hydrocarbon molecules in the interfacial region.[25] They further expanded this line of work by investigating CO_2-regulated C8 flow in both quartz and kerogen nanopores, showing that in quartz, CO_2 first undergoes competitive adsorption, extracting the initial hydrocarbon layer, reducing slip velocity, and only later mixing with the flowing region to lower fluid viscosity. On the other hand, in kerogen, CO_2 mixes readily with hydrocarbons without an initial adsorption stage, making viscosity reduction the dominant mechanism for enhanced transport of oil in kerogen pores.[26] Together, these studies illustrate how CO_2 adsorption and competitive displacement vary across mineral types, offering a molecular-level framework for understanding CO_2-enhanced oil recovery mechanisms in shale and tight reservoirs.

A separate study by Zhang et al. further extended the molecular-scale understanding of CO_2–hydrocarbon interactions by examining oil recovery from calcite nanopores in systems containing heavier components such as C10 and C19.[27] Their simulations showed that, in the absence of CO_2, a substantial portion of the oil, especially the heavier C19, is stored as adsorbed molecules on pore walls, and oil recovery proceeds primarily through surface-mediated transport along thin liquid films; leading to faster recovery of the lighter component and strong preferential production of C10. When CO_2 is injected under miscible conditions, however, the mechanism shifts: CO_2 rapidly displaces the adsorbed oil, mixes with hydrocarbons in the pore interior, and greatly increases the mobility of both components; accelerating recovery and reducing the strong selectivity toward the lighter C10 observed without gas injection.[27]

Zhang et al.'s work highlights how competitive adsorption, displacement of interfacial oil, and CO_2-induced viscosity reduction together govern the efficiency of CO_2-enhanced oil recovery (EOR) in nanoporous calcite, and how these interfacial processes are strongly influenced by pore size. It complements earlier studies on CO_2 behavior in mineral nanopores by demonstrating how CO_2 interacts not only with simple alkanes but also with mixtures of heavier hydrocarbons, thereby expanding the mechanistic picture of CO_2-assisted recovery in shale and tight formations.[25-27]

Malani and Ayappa[28] examined water adsorption on mica using GCMC simulations and reproduced adsorption isotherms that agreed well with experimental measurements, demonstrating that the SPC water model captures water uptake and film accurately, particularly at higher humidities. Their analysis revealed that water adsorption proceeds through three distinct stages governed by the increase in hydration of surface K^+ ions and the progressive layering of water. The first stage commences as water begins occupying sites within and just above the plane of K^+ ions. The second stage consists of redistribution of water molecules, while the third stage is signified by the rapid loading of more bulk-like water that produces a thick, disordered film.

Their structural analysis showed strongly bound, ordered water adjacent to the mica basal plane, more liquid-like and mobile water in the second layer, and increasingly disordered water beyond it, consistent with previous MD findings and with experimental observations.[28] Complementary experiments by Balmer et al. reinforced this molecular picture by showing that water initially binds at specific cation-associated sites, and the transition from convex isotherm behavior to more bulk-like adsorption corresponds to the hydration-induced mobility of the surface ions.[29] Together, these simulation and experimental studies provide a detailed view of how ion-specific interactions, hydration shell formation, and layer-by-layer structural evolution govern water uptake on mica surfaces.

Later, Cheng and Sun showed that water molecules adsorbed on mica exhibit pronounced orientational ordering within the first few molecular layers, with particularly strong alignment for molecules located within roughly 0.6 nm of the surface. [30] Their simulations demonstrated that the first two density peaks commonly observed in water density profiles correspond to a single, structured water monolayer tightly associated with the mica substrate. Beyond this region, the adsorbed film transitions to a multilayer configuration in which water continues to build upward through hydrogen bonding. These findings reinforce the view that the first hydration layer on mica is highly ordered and strongly influenced by surface cations, while subsequent layers gradually lose this ordering as the adsorbed film grows.[30]

Previous simulations have advanced our understanding of CO_2 and water adsorption on minerals under unsaturated conditions. However, many questions remain open. For example, while the development of water films on minerals with RH has been studied, most analyses were based on laterally and temporally averaged density profiles. In particular, the *three-dimensional*, *instantaneous* structure of the water film and its evolution with RH is not yet known. At a more fundamental level, whenever a water film develops on a mineral surface, water-solid and water-vapor interfaces form. However, because of the solid-like structure of the innermost adsorption layer, it is unclear under what conditions (e.g., RH or water film thickness) the water-vapor interface truly becomes a liquid-vapor interface and what impact it brings. For CO_2, previous works revealed that it is less competitive in adsorbing on kaolinite surfaces than water.[31] However, the co-adsorption of water and CO_2 on mineral surfaces received scant attention so far.[32, 33] How the RH in the environment quantitatively affects CO_2 adsorption, and if CO_2 adsorption still exists, how CO_2 molecules exist on the surface is not yet well understood. Further, how the presence of CO_2, especially at pressure relevant to subsurface applications, affects the adsorption of water on mineral surfaces has received little attention, let alone the underlying mechanisms.

In this thesis, we investigate the adsorption of pure CO_2, pure water vapor, and CO_2-water vapor mixture on mica surfaces using molecular simulations. The rest of the thesis is organized as follows. Chapter 3 presents the simulation system and methods. In Chapter 4, the adsorption of pure CO_2 and water vapor is discussed first, followed by the co-adsorption of CO_2 and water. The adsorption isotherms and structure of adsorbates are quantified and the underlying mechanisms analyzed. Finally, conclusions are drawn in Chapter 5.

Chapter 3. Simulation Systems, Models, and Methods

3.1 Molecular Systems

As shown in Figs. 5a, 5b, and 5c, systems A, B, and C are adopted to study the adsorption of CO_2, water vapor, and CO_2-water vapor mixture on mica ($KAl_2(AlSi_3O_{10})(OH)_2$) surfaces. Each system consists of two 2 nm-thick mica slabs and the specific fluids confined between them. The mica slabs measure 6.294 nm by 5.508 nm in the *x*- and *y*-directions, respectively. The separation between the surface K^+ ions of the two mica walls is 6 nm so the adsorption on one wall is independent of the other. Both mica walls are frozen during the simulations. A vacuum of 1.1 nm in height is placed above the top mica slab and below the bottom mica slab. Periodic boundary conditions are applied in the lateral (*x*-*y*) plane; the system's periodicity in the *z*-direction is removed (see Fig. 5). It is worth noting that the mica surface considered here is among the most hydrophilic surfaces in nature and water exhibits complete wetting on it.[34]

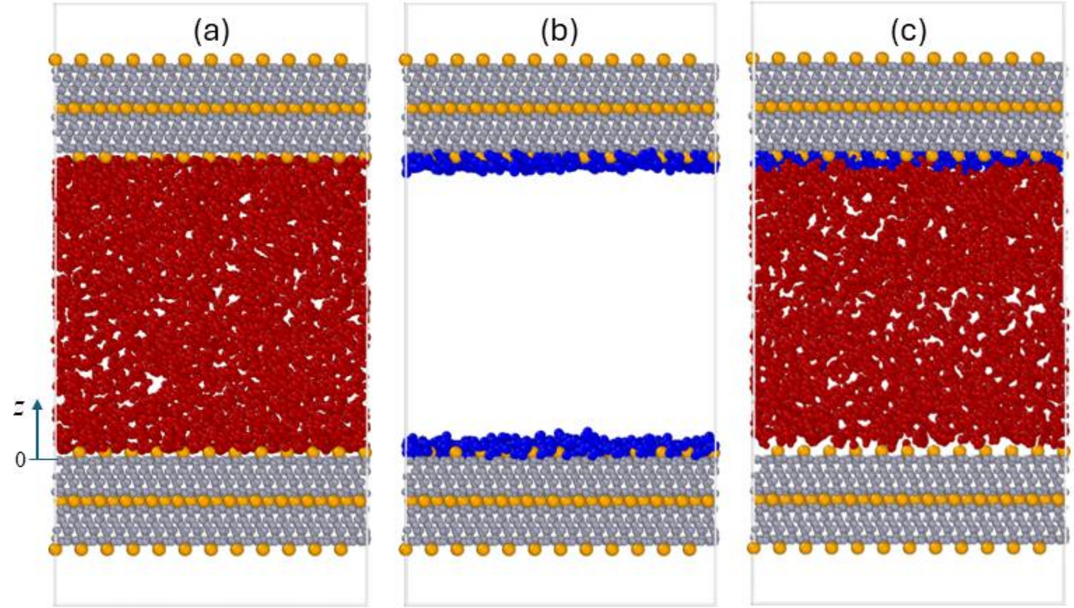

Fig. 5. Snapshots of molecular systems for studying adsorption of pure CO_2 (**a**), pure water (**b**), and CO_2 + water vapor mixture on mica (**c**). The origin of the z axis (*z* = 0) corresponds to the surface oxygen plane of the lower mica wall. In (c), to better delineate to what extent CO_2 molecules can approach mica (in particular, its surface K atoms), the water molecules within 0.6 nm of the lower mica surface are not shown. Water and CO_2 molecules are shown using blue and red ball-and-stick models. In mica, the K atoms are shown as yellow balls, and all other atoms are shown as grey balls.

The fluid temperature is maintained at 298.15K in all systems. The target pressure in systems A and C is controlled at 100 bar, which is relevant to the condition for CO_2 and H_2 underground storage, where pressure up to 200 bar can be encountered.[6, 11, 12] Because the system temperature is only slightly below CO_2's critical temperature (304.13K) and the target pressure is above the CO_2's critical temperature (73.77 bar), CO_2 in these systems is almost at the liquid-dense gas boundary. Such a fluid is expected to completely wet the mica surface due to its vanishing surface tension.

The partial pressure of water vapor in systems B and C is controlled at 10^{-4}, 10^{-2}, 0.1, 0.2, 0.4, 0.6, 0.8, and 0.9 times water's saturation pressure (P_0) at our target temperature, thus producing a relative humidity (RH) in the range of 0.01% to 90%. P_0 is set to 0.044 bar based on the water model we adopted and in accordance with prior GCMC studies.[28, 30, 35]

3.2 Molecular Models

The rigid SPC model[36] is used for water molecules and the CLAYFF force field[37] is selected for the mica substrate. Reactions of CO_2 are not considered. Previous simulations showed that these force fields together allow an accurate prediction of water adsorption on mica.[28, 30] We adopt the force field developed by Zhu *et al*[38] for CO_2 molecules because it captures the thermodynamic properties of CO_2 near the critical point and has been used extensively in studies of CO_2 adsorption on mineral surfaces.[18, 19, 21]

3.3 Simulation Methods

All simulations are performed using the LAMMPS code.[39] In systems A and B, the GCMC approach is used to control the pressure of fluids in the mica channel. In system C, the GCMC approach is used to control the partial pressure of water vapor but the CO_2 pressure is tuned to within 5% of the target pressure (100 bar) by adjusting the number of CO_2 molecules in the system through trial and error. Specifically, we compute the pressure of CO_2 by measuring the force acting on each mica slab and then add/remove CO_2 molecules from the system as needed to reach our target pressure. Note that, for system C, this approach is not exact because the contribution of water to pressure is included in the measured force and pressure. However, because water's partial pressure (at most 0.04 bar even at RH = 90%) is very low compared to the CO_2 pressure (100 bar), the error caused by water is negligible. GCMC runs are performed using the "fix gcmc" command in LAMMPS. In these runs, GCMC and MC operations are invoked every 100 MD steps, where an average of 10 exchange attempts with an equal probability of molecule translations or rotations are performed. Convergence is typically achieved in 15 ns, but extended runs of 30 ns are required for RH = 80% and 90% to ensure good convergence.

For each system, after the number of molecules in the system reaches equilibrium through GCMC runs, a separate system is set up with the average number of molecules measured in the GCMC runs. MD simulations are then performed using this system for 4 ns to gather statistics such as density profiles and molecule orientations.

For all systems, the temperature of fluids is maintained at 298.15 K with a Nose-Hoover thermostat. The non-electrostatic interactions are computed with a cutoff length of 1.2 nm. Electrostatic interactions are handled using the Particle-Particle Particle-Mesh (PPPM) method, with a real-space cutoff length of 1.2 nm and a relative accuracy of 10^{-4}. The slab correction is applied in the electrostatic calculations to effectively remove the system's periodicity in the *z*-direction. All simulations are conducted with a time step of 1 fs.

3.4 Interfacial Structure Analysis

The one-dimensional (1D) number density profiles of CO_2 and H_2O molecules are computed across the mica channel using the binning method in which a time-averaged histogram of molecules is obtained based on their z-position. Averaging over time and the lateral (xy-) dimensions produces a signal that can be easily compared between different systems, but doing so obscures details about the *instantaneous* and *three-dimensional* structure of the water film. To alleviate this limitation, we adopt the ITIM (Identification of the Truly Interfacial Molecules) analysis for several of the systems studied here to complement the 1D density profiles. An ITIM analysis seeks to reveal the structure of interfacial fluids by identifying successive layers of molecules at interfaces at each time instant.[40-42] As shown in Fig. 6, for the flat interface considered here, probing spheres (radius: R_{ps}) are moved from a bulk phase toward the interface along test lines normal to the interface till they touch atoms of interfacial fluids. The test lines are arranged into a grid (spacing: d_{G}). Once a probing sphere touches the first atom on its path (e.g., the light blue circle in Fig. 6), the molecule to which the atom belongs is marked to be at the interface and the method proceeds with moving the next probing sphere. Once the probing of the interface is completed, molecules identified to be at the interface (e.g., the blue circles in Fig. 6) are tagged as the first interfacial layer and deleted from the system. The process is then repeated to identify the next molecule layers near the interface (e.g., the green and magenta circles in Fig. 6). The above process offers a quantitative way to identify interfacial molecules. It is a powerful supplement to the 1D density profile and graphic rendering of snapshots of molecular systems widely used in literature. Because the process can be applied to many trajectory frames, ITIM also allows the number of water molecules in each interfacial layer to be averaged over many frames to improve statistics.

In this work, we use the open-source package PyTim,[43] which leverages the MD trajectory analysis package MDAnalysis,[44] to perform the ITIM analysis. A probing sphere radius of 0.125 nm and a grid spacing of 0.05 nm, values recommended for interfacial water by Jorge *et al.*,[45] are used to identify interfacial molecules. Near the lower mica wall, probing spheres are moved from below the mica upward and mica atoms are discarded in the ITIM process.

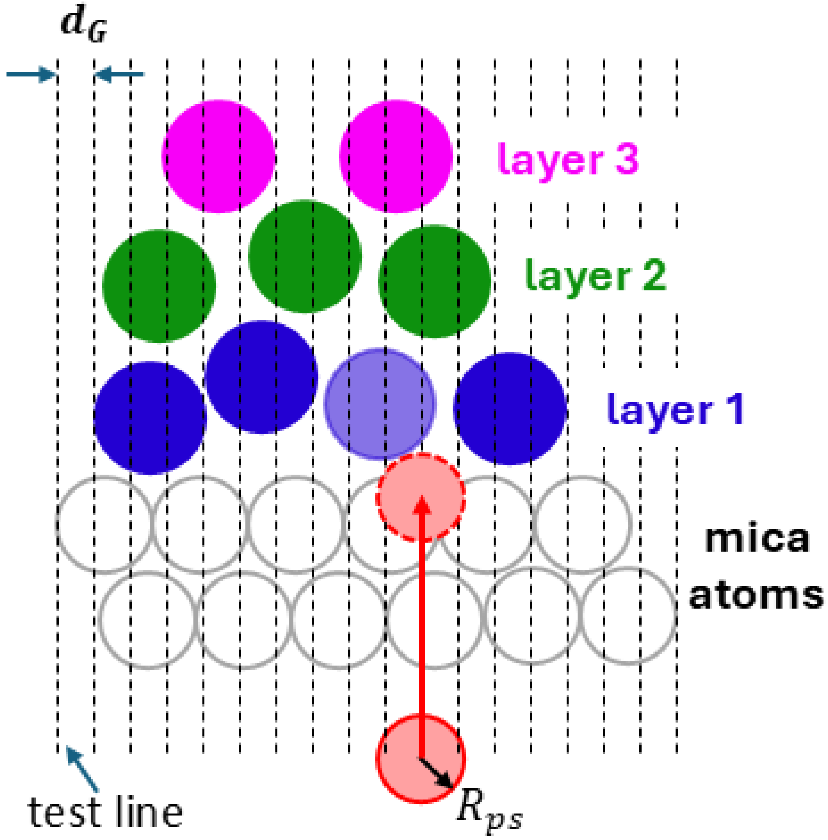

Fig. 6. A schematic for the determination of individual molecular layers adsorbed on a solid surface using the ITIM (Identification of the Truly Interfacial Molecules) methodology.

Chapter 4. Results and Discussion

4.1 Adsorption of Pure CO_2 and Water on Mica Surfaces

4.1.1 Pure CO_2

Figure 7 shows the density profile of CO_2 normal to the lower mica wall (density near the upper wall is not shown due to symmetry). Distinct layering, with three peaks centering at $z = 0.26$, 0.42, and 0.53 nm, is observed. Such layering is consistent with the structure of dense fluids near solid surfaces.[46] The first peak corresponds to the contact adsorption of CO_2 on mica's surface oxygen plane, and due to CO_2 molecules' relatively large size, it is located above the surface K^+ ions. The second peak corresponds to CO_2 molecules coordinating the surface K^+ ions and CO_2 molecules in the first density peak. The third peak, poorly differentiated from the second peak, represents CO_2 molecules in contact with the CO_2 molecules in the first two peaks.

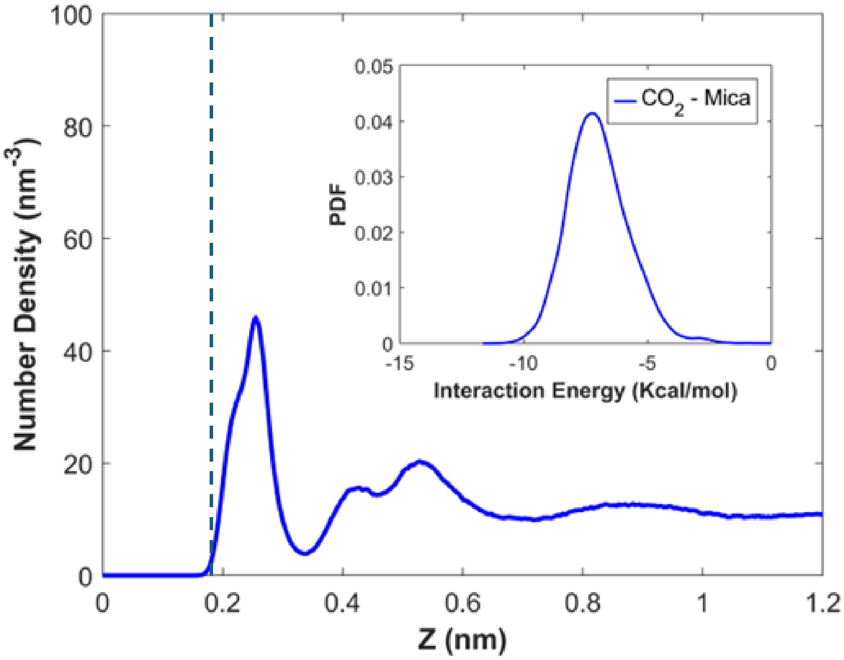

Fig. 7. Density profile of CO_2 near the lower mica wall when the CO_2 pressure is 100 bar. The vertical dashed line marks the position of surface K^+ ions. The inset is the distribution of the CO_2-mica interaction energy for CO_2 molecules in the first density peak. A CO_2 molecule's position is computed based on its carbon atom.

The significant first peak indicates strong adsorption of CO_2 molecules on the mica surface. In fact, such strong adsorption is driven mainly by the electrostatic interactions between mica's surface atoms and the CO_2 molecules. On the one hand, while CO_2 molecules are neutral and apolar, they have a large quadrupole moment (13.67×10^{-40} C·m^2).[47] On the other hand, the mica surface has a strong ionic nature and its atoms carry large partial charges. Consequently, the charge-quadrupole interactions between CO_2 molecules and mica surface atoms are strong. Such interactions are not screened by dielectric fluids in the dry environment considered here and thus lead to a strong affinity of CO_2 molecules to the mica surface. Indeed, Fig. 7's inset shows that the CO_2-mica interactions for the CO_2 molecules in the first peak can reach as much as -10 kcal/mol, which explains their strong adsorption (see Appendix I for the method for computing the interaction energy).

4.1.2 Pure Water

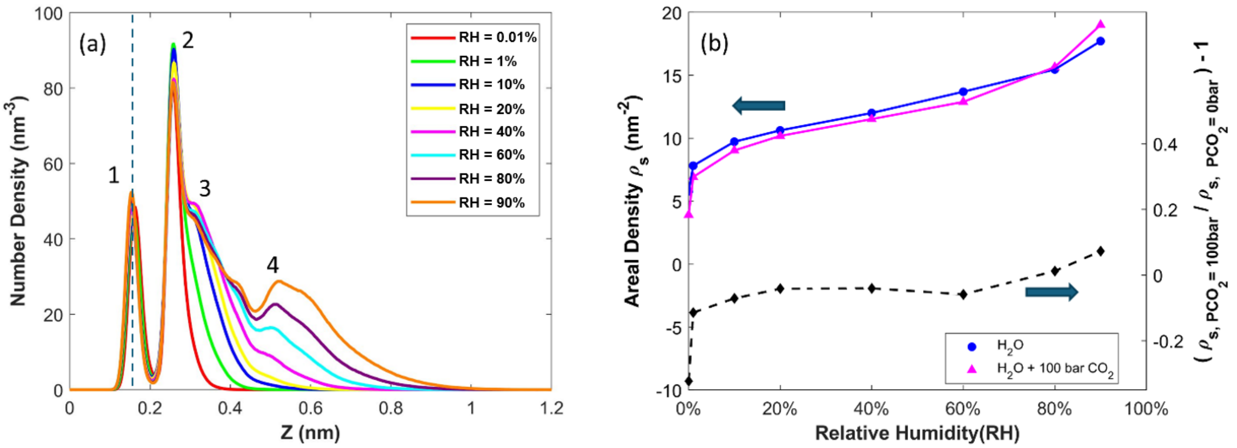

Fig. 8. (**a**) Density profiles of pure water near the lower mica wall when the relative humidity (RH) in the mica channel is varied. Water molecules' positions are computed based on their oxygen atoms. (**b**) The adsorption isotherms of water on mica in the absence and presence of a 100 bar CO_2 atmosphere. In (a), 1, 2, 3, and 4 mark the four main density peaks. Water density profiles in (a) are also shown in separate panels for different RHs in Fig. S1 Appendix II.

Figure 8a shows the density profiles of water near the lower mica wall ($z < 1.2$ nm) when the RH in the channel is varied between 0.01% and 90%. Figure 8b shows the corresponding water adsorption isotherm, with the adsorption computed by the integration of the water density profile from the mica's surface oxygen plane to $z = 1.2$ nm. These results closely follow those reported in previous molecular simulations (e.g., the isotherm at the RHs considered agrees with that reported earlier within an average difference of 3%), which agrees favorably with experimental data.[28-30] Therefore, below we only highlight their salient features briefly.

At RH = 0.01%, water already adsorbs on the mica surface to form two density peaks. This observation is consistent with the strongly hydrophilic nature of mica (e.g., water exhibits complete wetting on freshly cleaved mica surfaces).[34] The water molecules in the inner peak form hydrogen bonds with the basal oxygen atoms, while those in the second peak also hydrate the surface K^+ ions. As RH increases, the second density peak grows, and the third density peak begins to develop at RH $\approx$ 10%. The adsorption grows rapidly with RH up to 10%, with the increase of adsorption slows down as RH increases. As RH increases beyond 10%, the third peak grows, which is accompanied by the redistribution of water molecules between the second and the third density peaks. The adsorption grows slowly till RH reaches 60-80%. At RH beyond 60-80%, the third water density peak becomes fully developed, and a clear fourth peak emerges, and this is accompanied by the rapid growth of adsorption with RH.

While the 1D density profiles in Fig. 8a provide some information on the development of the nm-thick water film on the mica surface as the environmental RH increases, it offers little insight into the instantaneous, three-dimensional (3D) structure of the thin water film. To address this limitation, we scrutinize the development of individual water layers on the mica surface as RH increases using the ITIM methodology. Figures 9a-h show representative, top-view snapshots of individual water molecular layers atop the mica surface at RH of 0.01% to 90%.

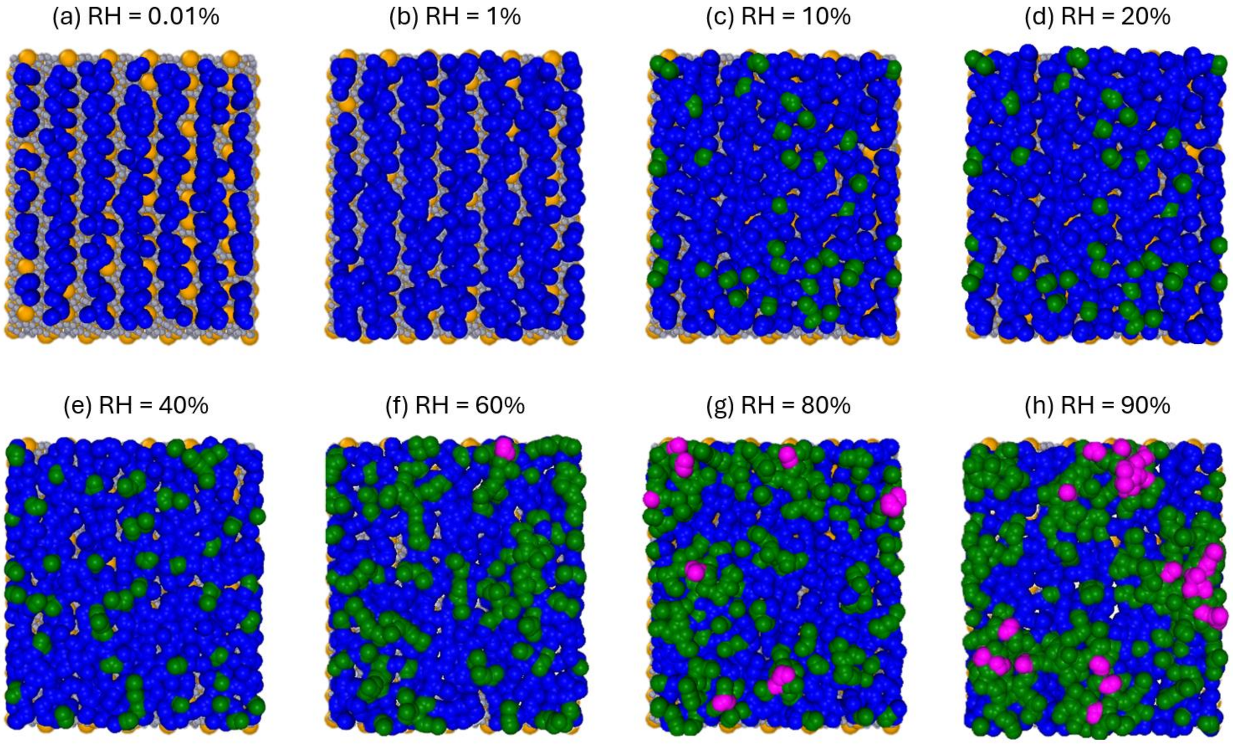

Fig. 9. (**a-h**) Representative snapshots of individual water layers atop mica surfaces with RH of 0.01% to 90% in the top view. The first layer, in contact with the mica wall, is colored blue. The second (third) water layer, positioned above the first (second) layer, is colored green (magenta). The surface K^+ ions are colored yellow.

At RH = 0.01%, the first water layer forms to mainly hydrate mica's surface oxygens and lies in the interstitial space between surface K^+ ions (Fig. 9a), consistent with earlier findings.[28, 30] As RH increases to 1%, more water molecules appear near the surface K^+ ions (Fig. 9b). Although these water molecules correspond to the second peak near the mica surface shown in Fig. 8a, they belong to the first water layer because there are no water molecules beneath them. As RH increases to 10%, the first water layer densifies further and a second water layer also emerges (Fig. 9c). At this stage, water molecules in the vapor phase "see" a heterogeneous surface featuring (1) a water layer in direct contact with the mica surface (cf. blue spheres in Fig. 9c) and (2) a second water layer (cf. green spheres in Fig. 9c) on top of the first water layer. Water molecules in the second layer form a coordination structure with those in the first layer but hardly associate with each other. The second water layer grows as RH increases (cf. Fig. 9c-e). When RH reaches 60-80%, the second water layer covers up most of the first water layer (cf. Fig. 9f-g), and molecules in them form contacts extensively.

At RH = 80%, a third layer featuring water molecules distributed sparsely over the second water layer appears (Fig. 9g). Water molecules in this third layer are only coordinated with molecules in the second water layer. As RH increases further to 90%, water molecules in the vapor phase mainly “see” the second water layer (Fig. 9h). Nevertheless, at any time instant, a notable fraction of the mica surface is still covered only by a single layer of water molecules, a fact difficult to discern from the 1D density profiles in Fig. 8a.

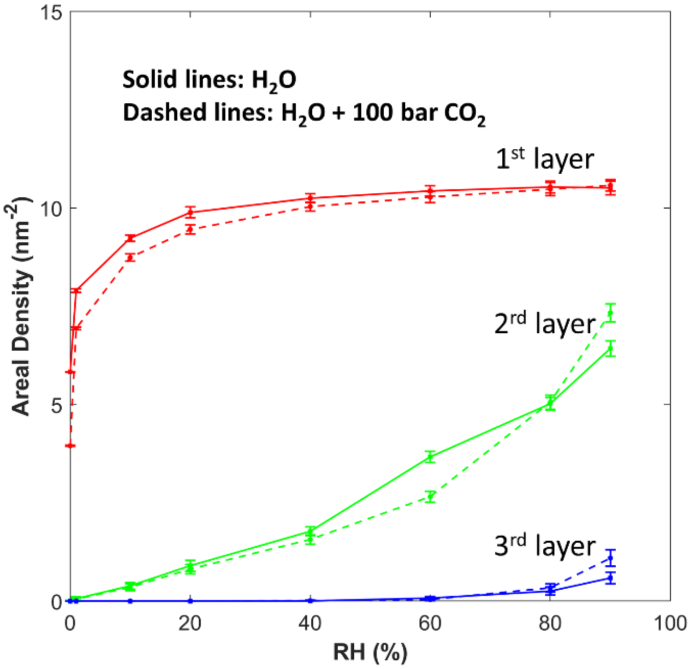

Fig. 10. The evolution of the areal density of the first, second, and third water layers atop the mica surface as a function of the environmental RH.

Figure 10 shows the evolution of the areal density of water molecules in different layers as the RH increases. The first water layer is well formed at RH = 20%. The second water layer still grows significantly at RH = 90%, while the third water layer emerges at an RH about 80%. Therefore, the growth of the thin water film at elevated RH occurs through the concurrent development of the second and third water layers. At RH = 90%, the areal density of the second water layer is about

70% of that of the first water layer, suggesting that some patches of the mica surface are still covered by a single layer of water molecules, which is consistent with the snapshot in Fig. 9h.

Overall, Figs. 9 and 10 reveal that the water film on top of a mica surface has a highly heterogeneous structure characterized by a different number of water molecule layers at different lateral positions. The structure revealed here and its evolution as a function of RH can have many ramifications. In the region where a mica surface is covered only by the first water layer, the water film is highly structured due to the strong water-mica interactions and distinct orientational ordering of water molecules (see Fig. S2). Further, water molecules in the first density peak exhibit sluggish dynamics (see Fig. S3), similar to that reported near mica walls enclosing bulk water.[48] Therefore, the water film behaves more like a solid (rather than a liquid) toward vapor phase molecules impinging on it. In regions where a mica surface is covered by an extensive second and even third water layers, in which water molecules of the same layer percolate well, molecules impinging toward the mica surface "see" a liquid-like boundary. It follows that, although a solid-water and a water-vapor interface form once a water film forms on the mica surface, the true liquid-vapor interface emerges only when the water film becomes well developed, e.g., at RH = 60%-80% according to Fig. 9f-g. The coverage of a mica surface by how many layers of water molecules and the emergence of a true liquid-vapor interface control the interfacial environment for other molecules (e.g., CO_2 molecules), and consequently can affect their adsorption and geochemical reactions.

4.2 Co-adsorption of CO_2 and Water on Mica Surfaces

4.2.1 Qualitative Features

Figure 11 shows the density profiles of CO_2 and water near the lower mica wall when the CO_2 pressure is fixed at 100 bar while the RH is varied from 0.01% to 90%. The water density profiles qualitatively resemble those for the pure water case (cf. Fig. 8), suggesting that environmental CO_2, even at a pressure of 100 bar, affects the water adsorption rather modestly. The CO_2 density profiles, however, differ greatly from those of the pure CO_2 case (cf. Fig. 7). At RH = 0.01%, the first CO_2 peak is lowered from the pure CO_2 case, although layering, evident from the second and third peaks, remains distinct. As RH increases, the first CO_2 peak is shifted away from the mica surface and its height reduces further. CO_2 layering, a key signature of solid-fluid interfaces, is maintained up to an RH of 40-60%. This trend is consistent with the fact that the water film presents a solid-vapor-like interface toward CO_2 molecules above it up to these RHs, a key conclusion from the ITIM analysis presented above. As RH increases beyond 60%, the CO_2 density decreases smoothly toward the mica surface, which is consistent with the emergence of a liquid-vapor interface above the mica surface at these RHs.

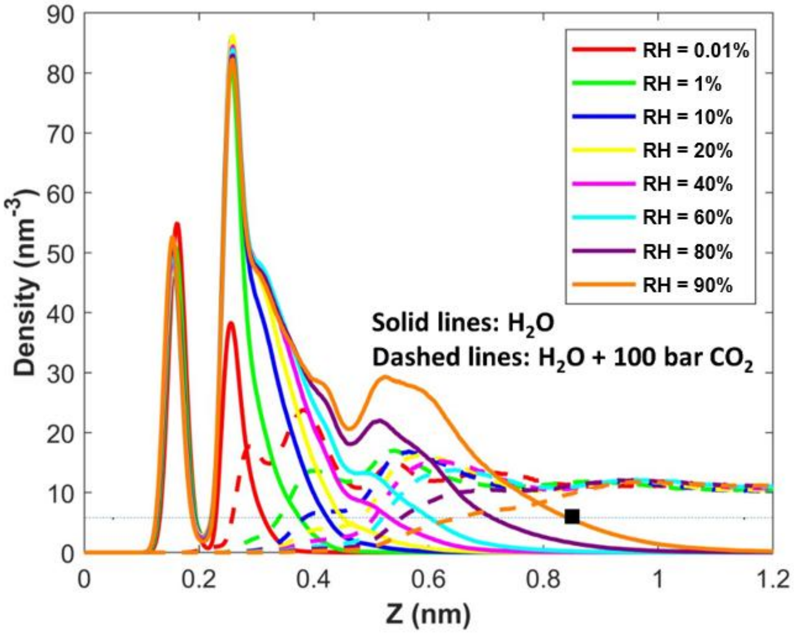

Fig. 11. Density profiles of CO_2 and water near the lower mica wall when the CO_2 environmental pressure is kept at 100 bar while RH is varied from 0.01% to 90%. Density profiles are also shown in separate panels for different RHs in Fig. S1 Appendix II.

4.2.2 Quantitative aspects of CO_2 adsorption

We first quantify the contact adsorption of CO_2 in the presence of water by integrating the CO_2 density from $z = 0$ to $z = 0.46$ nm. The latter position corresponds to the second valley of the CO_2 density profiles at RH = 0.01% and 1%, where CO_2 molecules are still in contact with the mica surface and there are few water molecules, if any, beneath them. Figure 12a shows that CO_2 adsorption is reduced by about 55% when water vapor with an RH of 0.01% is introduced above the mica surface. CO_2 contact adsorption is suppressed further as RH increases. At RH = 90%, when the water film is confined within 1 nm from the mica surface, CO_2 contact adsorption is reduced by about 99%.

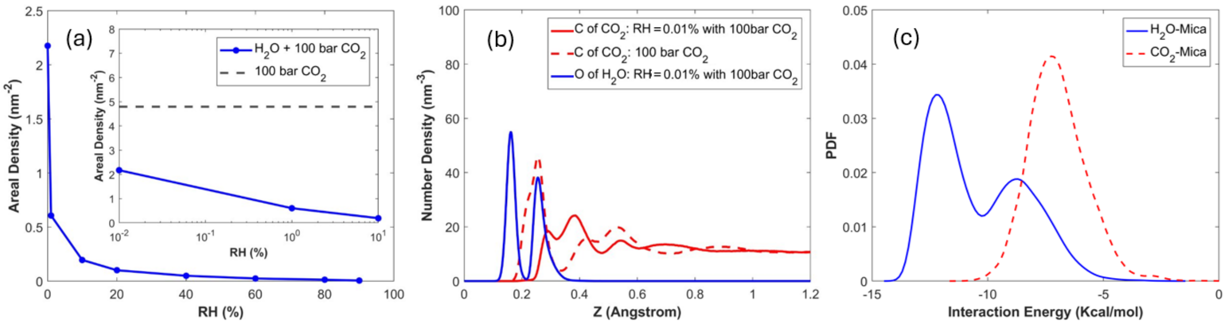

Fig. 12. (**a**) CO_2 adsorption isotherm as a function of the RH. (**b**) A comparison of the CO_2 density profile near the lower mica wall when the RH is 0 and 0.01%. (**c**) Distribution of the interaction energy of adsorbed CO_2 (p_{CO_2} = 100 bar, RH = 0) and water (p_{CO_2} = 0; RH = 0.01%) molecules with the mica wall.

A detailed picture of the suppressed CO_2 adsorption at low RHs can be obtained from the CO_2 and water density profiles at RH = 0.01%. Figure 12b shows that the thin water film pushes CO_2 away from the mica, but does not eliminate CO_2 adsorption. In fact, two clear contact adsorption peaks centering at $z = 0.29$ and 0.38 nm are still visible. The reduced CO_2 adsorption is attributed to the displacement by adsorbed water molecules, which is in turn caused by the stronger water-mica than CO_2-mica interactions. Figure 12c compares the distribution of the interaction energy for CO_2 molecules in the first adsorption peak in system A (i.e., no water in system) and the interaction energy for water molecules in system B (i.e., no CO_2 in system) at RH = 0.01% (see

Appendix I for the calculation of these energies). The water-mica interactions are generally much stronger than the CO_2-mica interactions because water molecules are smaller and highly polar, thereby allowing water molecules to displace CO_2 molecules from favorable spots on the mica surface. However, the partial overlap between CO_2-mica and water-mica interaction energy distributions reveals that CO_2-mica interactions are also strong, thereby explaining why CO_2 molecules are not fully displaced from the mica surface at RH = 0.01%.

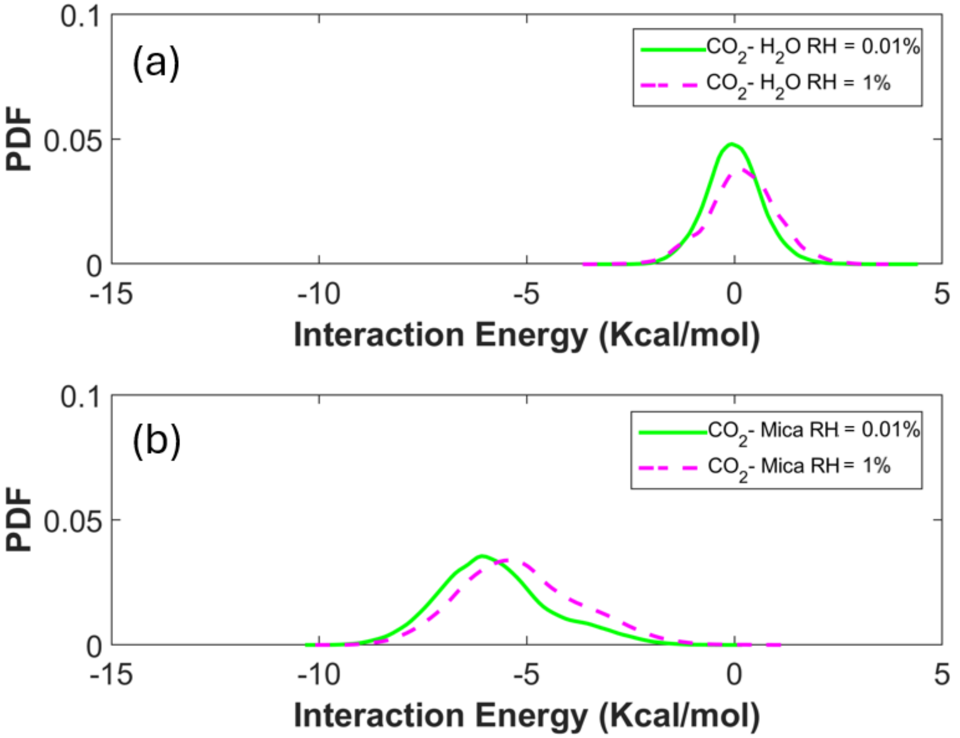

Fig. 13. Distribution of the interaction energy of contact adsorbed CO_2 molecule ($z < 0.32$ nm) with mica and water at RH of 0.01% and 1%. (a) CO_2-water interactions. (b) CO_2-mica interactions.

Another factor that may contribute to the weakened adsorption of CO_2 molecules is the dielectric screening of electrostatic CO_2-mica attractions by water. The direct assessment of this screening effect is difficult, but we can infer its role by quantifying the CO_2-mica and CO_2-water interactions at different RHs. Figures 13a and 13b show these interaction energies of CO_2 molecules located below $z = 0.32$ nm at RH = 0.01% and 1%. We observe that, as RH increases from 0.01% to 1% and thus more water adsorbs on the mica (cf. Fig. 8b), the CO_2-water interaction becomes generally more positive, and its mean value shifts by about +0.21 kcal/mol, lending support to the relevance of dielectric screening of CO_2-mica interactions. However, over the same RH window, the CO_2-mica interaction energy also becomes more positive, and its mean value shifts by about +0.59 kcal/mol. This suggests that CO_2 molecules are displaced from their favorable spots on the mica surface, and the larger magnitude of CO_2-mica interaction energy than the CO_2-water interaction energy shift shows that the dielectric screening effect is relatively minor. The latter is attributed to the fact that, at the low RH considered here, the dipole orientation of water molecules adsorbed on the mica surface is dominated by water-mica interactions.

The results presented above show that, in the presence of water vapor in the environment, small but nonzero contact adsorption CO_2 molecules can occur on the mica surface. Here, we examine the hydration environment of the contact-adsorbed CO_2 molecules, which can potentially affect the dynamics and chemical reactivity of those CO_2 molecules. Figure 14 shows the distribution of water around a CO_2 molecule contact adsorbed at $z = 0.4 \pm 0.04$ nm, where a CO_2 density peak is observed at RH = 0.01% and 1% (Fig. 11). Specifically, the density of water molecules is shown as a function of their *z*-position (Z) and distance from the CO_2 molecule's C atom (cf. the filled white semicircle) in the *xy*-plane (or the lateral direction, R). At RH = 0.01%, the CO_2 molecule is mainly hydrated by a layer of water around a solid angle θ of 135° (the solid angle is defined relative to the CO_2 molecules' C atom in the (R, Z) space, see Fig. 14). As RH increases (Fig. 14b-c), a second layer of hydration water appears just beneath the CO_2 molecule's equator. As RH increases beyond 60%, additional hydration water is introduced above the CO_2 molecule's equator (Fig 14. d-e). However, even at RH = 90%, when water molecules can reach $z = 1.0$ nm above the mica surface

(Fig. 11), hydration water does not reach a solid angle θ of less than 35°. Therefore, over the entire range of RH studied here, contact-adsorbed CO_2 molecules are not fully hydrated.

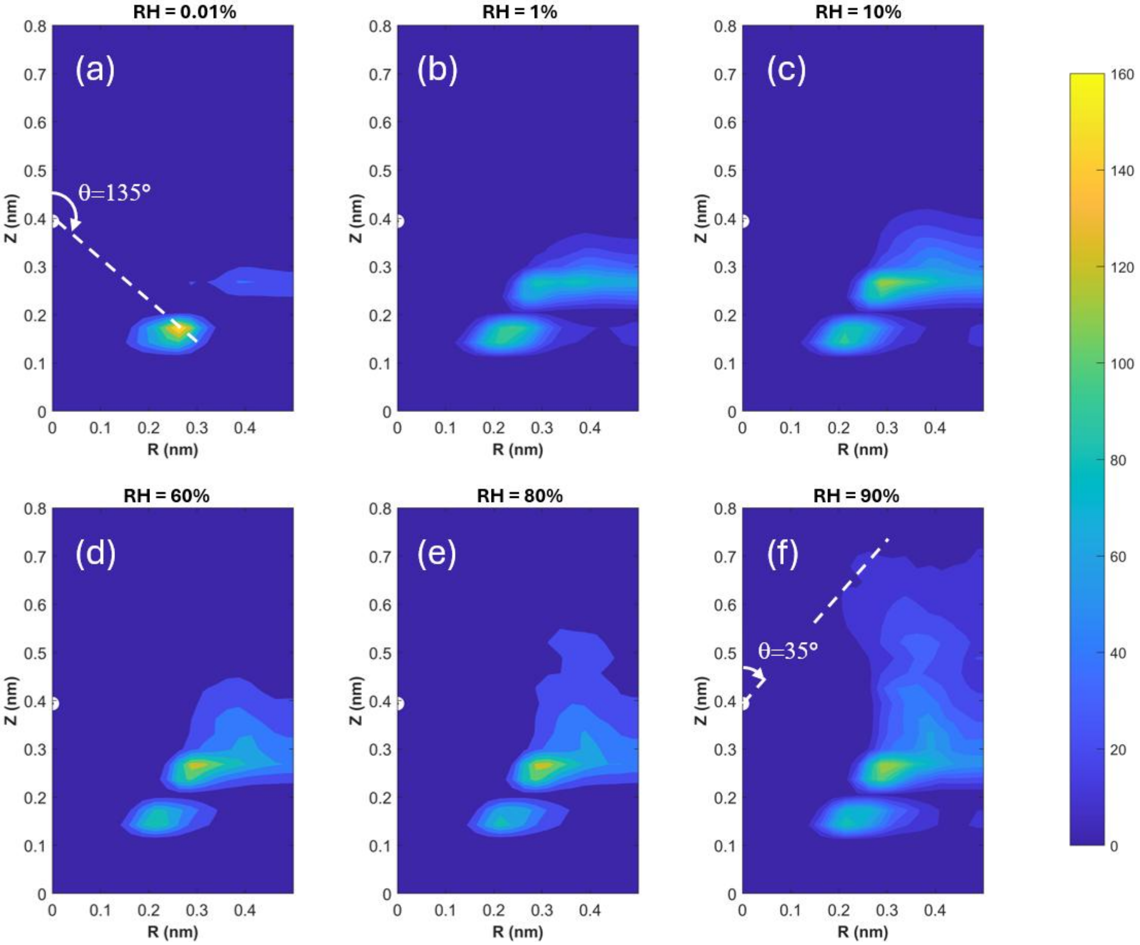

Fig. 14. Density distribution of water molecules around CO_2 molecules positioned at 0.4 nm above the mica surface at RH of 0.01% to 90%. The density is plotted as a function of the water molecules' *z*-position (Z) and their distance from the CO_2 molecule's C atom (cf. the filled white semicircle) in the *xy*-plane (i.e., the lateral direction, R). The CO_2 environmental pressure is 100 bar.

In this study, partial CO_2 dissolution and carbonic acid formation, which could influence adsorption behavior, are neglected because the force fields used in our simulations do not account for chemical reactions. Developing or incorporating reactive force fields in future studies would be necessary to fully capture the interplay between CO_2 dissolution, water adsorption, and potential chemical transformations, especially at RH higher than 90%.

4.2.3 Quantitative aspects of water adsorption

Figure 8b shows the effects of 100 bar CO_2 on the water adsorption isotherm, and Fig. 10 shows the change of the areal density of each true interfacial water layer induced by 100 bar CO_2. (The water density profiles in the CO_2-free and 100 bar-CO_2 systems are presented side by side in Fig. S1 to show their subtle differences, and their comparisons will be highlighted below whenever necessary.) The modulation of water adsorption by 100 bar CO_2 can be classified into three stages.

In the first stage (RH = 0.01% to 20%), a significant (32.29%) reduction of adsorption occurs at RH = 0.01%. This reduction of adsorption becomes less significant as RH increases. The region in which water loss occurs shifts slightly away from the mica surface (Fig. S1a-d). In the second stage (RH = 20% to 60%), only a minor reduction of adsorption occurs and it is insensitive to the RH. In the last stage (RH = 60% to 90%), the water adsorption gradually switches from reduction to enhancement. At RH = 90%, a modest enhancement of water adsorption (7.26%) occurs. This enhancement is achieved by the addition of water molecules to the second and third true water layers on the mica surface (Fig. 10) and occurs in the region $z > 0.65$ nm (Fig. S1h).

These results suggest that high-pressure CO_2 has a discernible effect on water adsorption at very low and high RHs, conditions that can occur in unsaturated tight media in applications such as CO_2 sequestration and CO_2-cushioned H_2 storage in depleted unconventional reservoirs. To understand the above three stages of evolution, we note that, for a mica surface in equilibrium with water vapor, introducing high-pressure CO_2 in the environment modulates water adsorption through three key mechanisms.

First, CO_2 can reduce water adsorption via two mechanisms: (1) it squeezes away water molecules from the water film on the mica and (2) it disrupts water-water associations. The former is akin to the thinning of water film confined between two solid surfaces under the action of external pressures applied on those surfaces. In the latter, CO_2 molecules get between adsorbed water molecules to disrupt their association and thus suppress their adsorption. The film squeezing and water dissociation effects are countered by mica-water and water-water interactions, which for the water film thickness here ($\lesssim 1$ nm), can be called the hydration effects. Second, CO_2 molecules can reduce water adsorption through surface displacement: because CO_2 molecules also interact strongly with mica (see Fig. 12c), they can displace some adsorbed water molecules. Third, direct CO_2-water interactions can increase water adsorption. van der Waals CO_2-water interactions can lower interfacial water molecules' potential energy to stabilize them energetically. Further, the collision with interfacial CO_2 molecules affords water molecules at the liquid-vapor interface more freedom in orientation, thereby stabilizing them entropically. Although all three mechanisms can act in each stage, their importance varies with RH, leading to the overall effects of environmental CO_2 on water adsorption shown in Fig. 8b.

In the first stage (RH < 20%), the reduction of water adsorption is contributed mainly by the first two mechanisms. In particular, CO_2 surface displacement plays a critical role because, as shown in Fig. 10 and Fig. S1a-d, the water loss at RH < 20% occurs via the removal of molecules in the region 0.21-0.4 nm, or equivalently, in the first true water layer on the mica surface (i.e., contact adsorbed water). Such removal is consistent with the displacement of water from the mica surface by contact-adsorbed CO_2 molecules. Indeed, Fig. 12a shows that a no amount of CO_2 molecules exist on the mica surface up to an RH of 20%.

In the second stage (RH = 20%-60%), the role of CO_2 surface displacement in the reduction of water adsorption gradually diminishes as RH rises since CO_2 contact adsorption vanishes rapidly (Fig. 12a). The environmental CO_2 is found to remove the water molecules in the tail region of the water density profile, which belongs to the second true water layer atop the mica surface (Figs.

S1e-f and Fig. 7). Such a water removal is mainly contributed by the water film squeezing and disruption of water-water association by CO_2. For example, at RH = 60%, the second true water layer already emerges but molecules in this layer do not associate extensively with each other, leaving them poorly coordinated and susceptible to the removal by environmental CO_2.

In the final stage, as RH increases from 60% to 90%, CO_2 surface displacement no longer affects water adsorption. The weakening of water-water association by CO_2 still suppresses water adsorption. Meanwhile, the enhancement of water adsorption driven by direct CO_2-water interactions becomes important near the water-vapor interface (or, near the tail of the water density profile, see Figs. S1g-h). To appreciate this, we examine the orientation ordering and interaction energy of the water molecules located at positions where the mean water density is 5.65 nm^{-3} (cf. black squares in Fig. 11; this position is selected as a representative position of water molecules directly exposed to the vapor phase (see Fig. S4 Appendix III). Figures 15a-b show that introducing 100 bar CO_2 above the water film with RH = 90% makes the orientation of water molecules near the liquid-vapor interface more random, which favor water adsorption. Furthermore, 100 bar-CO_2 atmosphere enhances molecules' total potential energy near the interface by 0.42 kcal/mol, which also favors water adsorption. We note that introducing CO_2 weakens water molecules' potential energy contributed through water-water interactions by 0.50 kcal/mol, but this is compensated by the potential energy gain of 0.95 kcal/mol due to the appearance of CO_2-water interactions (see Fig. S5).

The suppression of water adsorption through the disruption of water-water association by CO_2 becomes weaker as RH increases. This is because, as RH increases, the second and third true water layers atop the mica surface become more developed, with molecules in them becoming associated with more water molecules. The latter makes the disruption of their associations by CO_2 more difficult. On the other hand, the enhancement of water adsorption by direct CO_2-water interactions is not as sensitive (see Fig. S5). Consequently, their overall effect on water adsorption is negative at RH = 60%, becomes nearly zero at 80%, and positive at RH = 90%.

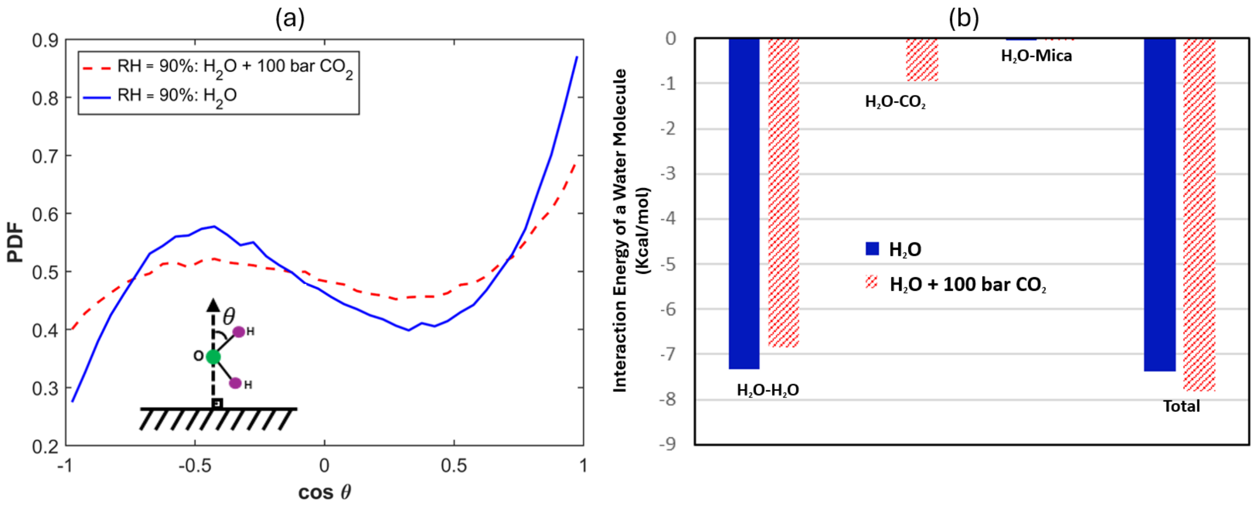

Fig. 15. (**a**) The orientation distribution of the OH bond of water molecules located at the position where the water density is 5.65 nm^{-3} (cf. the filled black circles in Fig. 10). Solid (dashed) lines are for situations with CO_2 pressure of 100 bar (0 bar). (**b**) The average interaction energy of water molecules located at the position where the water density is 5.65 nm^{-3}.

Chapter 5. Conclusions

The adsorption of pure CO_2, water, and their mixture on mica surfaces at unsaturated conditions is investigated. Water adsorption at RH = 0.01%-90% is found to be stronger than the CO_2 adsorption at 100 bar. A sub-nm water film readily forms on the mica surface at relatively low RH, leading to apparent liquid-solid and liquid-vapor interfaces at RH = 0.01%. ITIM analysis reveals that the film is spatially heterogeneous, predominantly featuring patches of 1-3 layers of water molecules across the mica surface even at an RH of 90%. Because the first true water layer atop the mica is highly constrained and water molecules in further interfacial layers are not well coordinated with others at low RH, a true liquid-vapor interface likely emerges only as RH approaches 60%-80%. The co-adsorption of CO_2 and water is characterized by the strong suppression of CO_2 contact adsorption. However, 100-bar CO_2 also lowers water adsorption by ~30% at RH = 0.01% due to CO_2's surface displacement effect. This suppression is weakened as RH increases and water adsorption becomes enhanced by about 7% at RH = 90%. This transition is attributed to the diminished CO_2 surface displacement, the weakening of CO_2's water film squeezing and water-water association disruption effects, and the stabilization of water at liquid-vapor interfaces by direct CO_2-water interactions at high RH.

While the present study focuses on the CO_2-water-mica system, its insights help understand the adsorption in other systems. The molecular structure of the heterogeneous water films on other mineral surfaces should show similar features as revealed here and the true liquid-vapor interfaces in those systems are expected to emerge only at higher relative humidity. Understanding such structures and interfaces aids in analyzing mass transfer at these interfaces (e.g., the value of the accommodation coefficient). The thermodynamics of the co-adsorption of CO_2 and water, especially the three mechanisms discussed above, can help understand the adsorption of multiple species on mineral surfaces. For example, given H_2's low density and its weaker interactions with mineral surfaces and water molecules, surface displacement, disruption of water-water association, and direct H_2-water interactions all should be considerably weaker than the CO_2 scenario studied here. Hence, we expect H_2 to affect water adsorption on mineral surfaces only marginally. To what extent these expectations remain true is of interest in the scenario of underground hydrogen storage, which may be explored in future studies.

The insights from the present research have important implications for subsurface energy and environmental technologies. For example, the fact that a minute amount of water can suppress the adsorption of CO_2 molecules on mica surfaces suggests that, contrary to predictions based on the assumption of a *completely* dry environment, adsorption may not contribute notably to the CO_2 storage capacity of depleted unconventional reservoirs even if the overall water saturation in the reservoir is far less than 100%. Furthermore, the fact that high-pressure CO_2 can reduce the water adsorption on mica surfaces at very low relative humidity (e.g., RH = 0.01%) suggests that the swelling of mica under very dry conditions can be suppressed by interstitial CO_2. The latter can compromise the mechanical integrity of caprocks in underground hydrogen storage sites, negatively impact gas retention and elevate leakage risks. These implications warrant experimental studies in the future.

References

(1) De Silva, G. P. D.; Ranjith, P. G.; Perera, M. S. A. Geochemical aspects of CO2 sequestration in deep saline aquifers: A review. *Fuel* **2015**, *155*, 128-143. DOI: https://doi.org/10.1016/j.fuel.2015.03.045.

(2) Wang, C.; Wu, S.; Shen, Y.; Li, X. Review on CO2–Brine Interaction in Oil and Gas Reservoirs. *In Energies*, **2024**; Vol. 17, p 3926. DOI: https://doi.org/10.3390/en17163926.

(3) Saran, R. CO2 Sequestration by Mineral Carbonation: A Review. *Global NEST Journal* **2018**, *20* (3), 497-503. DOI: https://doi.org/10.30955/gnj.002597.

(4) Luo, A.; Li, Y.; Chen, X.; Zhu, Z.; Peng, Y. Review of CO2 sequestration mechanism in saline aquifers. *Natural Gas Industry B* **2022**, *9* (4), 383-393. DOI: https://doi.org/10.1016/j.ngib.2022.07.002.

(5) Busch, A.; Bertier, P.; Gensterblum, Y.; Rother, G.; Spiers, C. J.; Zhang, M.; Wentinck, H. M. On sorption and swelling of CO2 in clays. *Geomechanics and Geophysics for Geo-Energy and Geo-Resources* **2016**, *2* (2), 111-130. DOI: 10.1007/s40948-016-0024-4.

(6) Zivar, D.; Kumar, S.; Foroozesh, J. Underground hydrogen storage: A comprehensive review. *International Journal of Hydrogen Energy* **2021**, *46* (45), 23436-23462. DOI: https://doi.org/10.1016/j.ijhydene.2020.08.138.

(7) Pan, B.; Yin, X.; Ju, Y.; Iglauer, S. Underground hydrogen storage: Influencing parameters and future outlook. *Advances in Colloid and Interface Science* **2021**, *294*, 102473. DOI: https://doi.org/10.1016/j.cis.2021.102473.

(8) Miocic, J.; Heinemann, N.; Edlmann, K.; Scafidi, J.; Molaei, F.; Alcalde, J. Underground hydrogen storage: a review. In *Enabling Secure Subsurface Storage in Future Energy Systems*; Geological Society of London, **2023**; p 0. DOI: 10.1144/SP528-2022-88.

(9) Hamed, H.; Reza, A.; Shahin, R.; Manouchehr, H.; Martin, J. B. Review of underground hydrogen storage: Concepts and challenges. *Advances in Geo-Energy Research* **2022**, *7* (2), 111-131. DOI: (acccessed 2025/11/20).

(10) Ren, J.; Sun, L.; Li, X.; Wang, P.; Jiang, L.; Song, Y. Interfacial dynamics and mass transfer in underground hydrogen storage applications: A review of H_2 flow, stability and storage performance. *Advances in Geo-Energy Research* **2025**, *18* (2), 121-136. DOI: https://ager.yandypress.com/index.php/2207-9963/article/view/615 (acccessed 2025/11/20).

(11) Heinemann, N.; Alcalde, J.; Miocic, J. M.; Hangx, S. J. T.; Kallmeyer, J.; Ostertag-Henning, C.; Hassanpouryouzband, A.; Thaysen, E. M.; Strobel, G. J.; Schmidt-Hattenberger, C.; et al. Enabling large-scale hydrogen storage in porous media – the scientific challenges. *Energy & Environmental Science* **2021**, *14* (2), 853-864, 10.1039/D0EE03536J. DOI: 10.1039/D0EE03536J.

(12) Abdolhosseini Qomi, M. J.; Miller, Q. R. S.; Zare, S.; Schaef, H. T.; Kaszuba, J. P.; Rosso, K. M. Molecular-scale mechanisms of CO2 mineralization in nanoscale interfacial water films. *Nature Reviews Chemistry* **2022**, *6* (9), 598-613. DOI: 10.1038/s41570-022-00418-1.

(13) Li, Y.; Narayanan Nair, A. K.; Kadoura, A.; Yang, Y.; Sun, S. Molecular Simulation Study of Montmorillonite in Contact with Water. *Industrial & Engineering Chemistry Research* **2019**, *58* (3), 1396-1403. DOI: 10.1021/acs.iecr.8b05125.

(14) Chen, Z.; Hu, L. Adsorption behavior of benzene on clay mineral surfaces at different temperatures and air humidity based on molecular simulation. *Applied Clay Science* **2023**, *243*, 107068. DOI: https://doi.org/10.1016/j.clay.2023.107068.

(15) Chen, G.; Lu, S.; Zhang, J.; Xue, Q.; Han, T.; Xue, H.; Tian, S.; Li, J.; Xu, C.; Pervukhina, M. Keys to linking GCMC simulations and shale gas adsorption experiments. *Fuel* **2017**, *199*, 14-21. DOI: https://doi.org/10.1016/j.fuel.2017.02.063.

(16) Hui, D.; Li, L.; Zhang, Y.; Peng, X.; Li, T.; Jia, C.; Pan, Y. Molecular simulation of adsorption behaviors of methane and carbon dioxide on typical clay minerals. *Frontiers in Energy Research* **2023**, *11*, Original Research. DOI: 10.3389/fenrg.2023.1231338.

(17) Ali, M.; Pan, B.; Yekeen, N.; Al-Anssari, S.; Al-Anazi, A.; Keshavarz, A.; Iglauer, S.; Hoteit, H. Assessment of wettability and rock-fluid interfacial tension of caprock: Implications for hydrogen and carbon dioxide geo-storage. *International Journal of Hydrogen Energy* **2022**, *47* (30), 14104-14120. DOI: https://doi.org/10.1016/j.ijhydene.2022.02.149.

(18) Peng, F.; Xiong, K.; Wang, R.; Li, Y.; Guo, Z.; Feng, G. Molecular Insight into Microbehaviors of n-Decane and CO2 in Mineral Nanopores. *Energy & Fuels* **2020**, *34* (3), 2925-2935. DOI: 10.1021/acs.energyfuels.9b04125.

(19) Wang, R.; Peng, F.; Song, K.; Feng, G.; Guo, Z. Molecular dynamics study of interfacial properties in CO2 enhanced oil recovery. *Fluid Phase Equilibria* **2018**, *467*, 25-32. DOI: https://doi.org/10.1016/j.fluid.2018.03.022.

(20) Santos, M. S.; Franco, L. F. M.; Castier, M.; Economou, I. G. Molecular Dynamics Simulation of n-Alkanes and CO2 Confined by Calcite Nanopores. *Energy & Fuels* **2018**, *32* (2), 1934-1941. DOI: 10.1021/acs.energyfuels.7b02451.

(21) Moh, D. Y.; Fang, C.; Yin, X.; Qiao, R. Interfacial CO2-mediated nanoscale oil transport: from impediment to enhancement. *Physical Chemistry Chemical Physics* **2020**, *22* (40), 23057-23063. DOI: 10.1039/d0cp03930f.

(22) Du, J.; Zhou, A.; Zhong, Y.; Shen, S.-L. Molecular simulation on CO2 adsorption heterogeneity in montmorillonite nanopores with different surface charges in presence of water. *Chemical Engineering Journal* **2024**, *482*, 148958. DOI: https://doi.org/10.1016/j.cej.2024.148958.

(23) Jin, Z.; Firoozabadi, A. Methane and carbon dioxide adsorption in clay-like slit pores by Monte Carlo simulations. *Fluid Phase Equilibria* **2013**, *360*, 456-465. DOI: https://doi.org/10.1016/j.fluid.2013.09.047.

(24) Moh, D. Y.; Zhang, H.; Sun, S.; Qiao, R. Molecular anatomy and macroscopic behavior of oil extraction from nanopores by CO2 and CH4. *Fuel* **2022**, *324*, 124662. DOI: https://doi.org/10.1016/j.fuel.2022.124662.

(25) Zhang, W.; Feng, Q.; Wang, S.; Xing, X.; Jin, Z. CO2-regulated octane flow in calcite nanopores from molecular perspectives. *Fuel* **2021**, *286*, 119299. DOI: https://doi.org/10.1016/j.fuel.2020.119299.

(26) Zhang, W.; Dai, C.; Chen, Z.; He, Y.; Wang, S. Recovery mechanisms of shale oil by CO2 injection in organic and inorganic nanopores from molecular perspective. *Journal of Molecular Liquids* **2024**, *398*, 124276. DOI: https://doi.org/10.1016/j.molliq.2024.124276.

(27) Zhang, H.; Wang, S.; Wang, X.; Qiao, R. Enhanced Recovery of Oil Mixtures from Calcite Nanopores Facilitated by CO2 Injection. *Energy & Fuels* **2024**, *38* (6), 5172-5182. DOI: 10.1021/acs.energyfuels.3c05235.

(28) Malani, A.; Ayappa, K. G. Adsorption Isotherms of Water on Mica: Redistribution and Film Growth. *The Journal of Physical Chemistry B* **2009**, *113* (4), 1058-1067. DOI: 10.1021/jp805730p.

(29) Balmer, T. E.; Christenson, H. K.; Spencer, N. D.; Heuberger, M. The Effect of Surface Ions on Water Adsorption to Mica. *Langmuir* **2008**, *24* (4), 1566-1569. DOI: 10.1021/la702391m.

(30) Cheng, T.; Sun, H. Adsorption of Ethanol Vapor on Mica Surface under Different Relative Humidities: A Molecular Simulation Study. *The Journal of Physical Chemistry C* **2012**, *116* (31), 16436-16446. DOI: 10.1021/jp3020595.

(31) Xia, Y.; Cai, M.; Wang, Y.; Sun, Q.; Dai, Z. Competitive adsorption mechanisms of multicomponent gases in kaolinite under electric fields: A molecular perspective. *Geoenergy Science and Engineering* **2024**, *238*, 212897. DOI: https://doi.org/10.1016/j.geoen.2024.212897.

(32) Zhang, M.; Jin, Z. Molecular simulation on CO2 adsorption in partially water-saturated kaolinite nanopores in relation to carbon geological sequestration. *Chemical Engineering Journal* **2022**, *450*, 138002. DOI: https://doi.org/10.1016/j.cej.2022.138002.

(33) Kadoura, A.; Narayanan Nair, A. K.; Sun, S. Adsorption of carbon dioxide, methane, and their mixture by montmorillonite in the presence of water. *Microporous and Mesoporous Materials* **2016**, *225*, 331-341. DOI: https://doi.org/10.1016/j.micromeso.2016.01.010.

(34) Metya, A.; Ghose, D.; Ray, N. R. Development of hydrophobicity of mica surfaces by ion beam sputtering. Applied Surface Science **2014**, 293, 18-23. DOI: https://doi.org/10.1016/j.apsusc.2013.11.163.

(35) Liu, J. C.; Monson, P. A. Does Water Condense in Carbon Pores? *Langmuir* **2005**, *21* (22), 10219-10225. DOI: 10.1021/la0508902.

(36) Berendsen, H. J. C.; Postma, J. P. M.; van Gunsteren, W. F.; Hermans, J. Interaction Models for Water in Relation to Protein Hydration. In *Intermolecular Forces: Proceedings of the Fourteenth Jerusalem Symposium on Quantum Chemistry and Biochemistry Held in Jerusalem, Israel, April 13–16, 1981*, Pullman, B. Ed.; Springer Netherlands, 1981; pp 331-342.

(37) Cygan, R. T.; Liang, J.-J.; Kalinichev, A. G. Molecular Models of Hydroxide, Oxyhydroxide, and Clay Phases and the Development of a General Force Field. *The Journal of Physical Chemistry B* **2004**, *108* (4), 1255-1266. DOI: 10.1021/jp0363287.

(38) Zhu, A.; Zhang, X.; Liu, Q.; Zhang, Q. A Fully Flexible Potential Model for Carbon Dioxide. *Chinese Journal of Chemical Engineering* **2009**, *17* (2), 268-272. DOI: https://doi.org/10.1016/S1004-9541(08)60204-9.

(39) Plimpton, S. Fast Parallel Algorithms for Short-Range Molecular Dynamics. *Journal of Computational Physics* **1995**, *117* (1), 1-19. DOI: https://doi.org/10.1006/jcph.1995.1039.

(40) Pártay, L. B.; Hantal, G.; Jedlovszky, P.; Vincze, Á.; Horvai, G. A new method for determining the interfacial molecules and characterizing the surface roughness in computer simulations. Application to the liquid–vapor interface of water. *Journal of Computational Chemistry* **2008**, *29* (6), 945-956. DOI: https://doi.org/10.1002/jcc.20852.

(41) Lbadaoui-Darvas, M.; Idrissi, A.; Jedlovszky, P. Computer Simulation of the Surface of Aqueous Ionic and Surfactant Solutions. *The Journal of Physical Chemistry B* **2022**, *126* (4), 751-765. DOI: 10.1021/acs.jpcb.1c08553.

(42) Fábián, B.; Senćanski, M. V.; Cvijetić, I. N.; Jedlovszky, P.; Horvai, G. Dynamics of the Water Molecules at the Intrinsic Liquid Surface As Seen from Molecular Dynamics Simulation and Identification of Truly Interfacial Molecules Analysis. *The Journal of Physical Chemistry C* **2016**, *120* (16), 8578-8588. DOI: 10.1021/acs.jpcc.5b10370.

(43) Sega, M.; Hantal, G.; Fábián, B.; Jedlovszky, P. Pytim: A python package for the interfacial analysis of molecular simulations. *Journal of Computational Chemistry* **2018**, *39* (25), 2118-2125. DOI: https://doi.org/10.1002/jcc.25384.

(44) Michaud-Agrawal, N.; Denning, E. J.; Woolf, T. B.; Beckstein, O. MDAnalysis: A toolkit for the analysis of molecular dynamics simulations. *Journal of Computational Chemistry* **2011**, *32* (10), 2319-2327. DOI: https://doi.org/10.1002/jcc.21787.

(45) Jorge, M.; Jedlovszky, P.; Cordeiro, M. N. D. S. A Critical Assessment of Methods for the Intrinsic Analysis of Liquid Interfaces. 1. Surface Site Distributions. *The Journal of Physical Chemistry C* **2010**, *114* (25), 11169-11179. DOI: 10.1021/jp101035r.

(46) Israelachvili, J. N. *Intermolecular and Surface Forces*; Academic Press, 2011. DOI: https://doi.org/10.1016/B978-0-12-375182-9.10029-6.

(47) Buckingham, A. D.; Disch, R. L.; Pople, J. A. The quadrupole moment of the carbon dioxide molecule. *Proceedings of the Royal Society of London. Series A. Mathematical and Physical Sciences* **1963**, *273* (1353), 275-289. DOI: doi:10.1098/rspa.1963.0088.

(48) Malani, A.; Ayappa, K. G. Relaxation and jump dynamics of water at the mica interface. *The Journal of Chemical Physics* **2012**, *136* (19), 194701. DOI: 10.1063/1.4717710 (acccessed 4/10/2025).

Appendices

Appendix I - Method for computing the interaction energies shown in Fig. 12c and 13

To compute the interaction energy between CO_2 and any species of interest (e.g., CO_2, mica, or H_2O molecules), LAMMPS' "rerun" command was used. For example, to determine components of CO_2's potential energy due to their interactions with mica, we loaded the trajectories saved during our original simulations but turned off the interactions between CO_2 and other species (CO_2 and H_2O) and used LAMMPS' "per/atom" command to evaluate CO_2-mica interactions for each CO_2 molecule in the system. Energy distribution can then be obtained through histograms. Documentations of LAMMPS' "rerun" and "pe/atom" commands can be found at https://docs.lammps.org/rerun.html and https://docs.lammps.org/compute_pe_atom.html

Appendix II - Density, orientation and dynamics of water molecules near mica surfaces

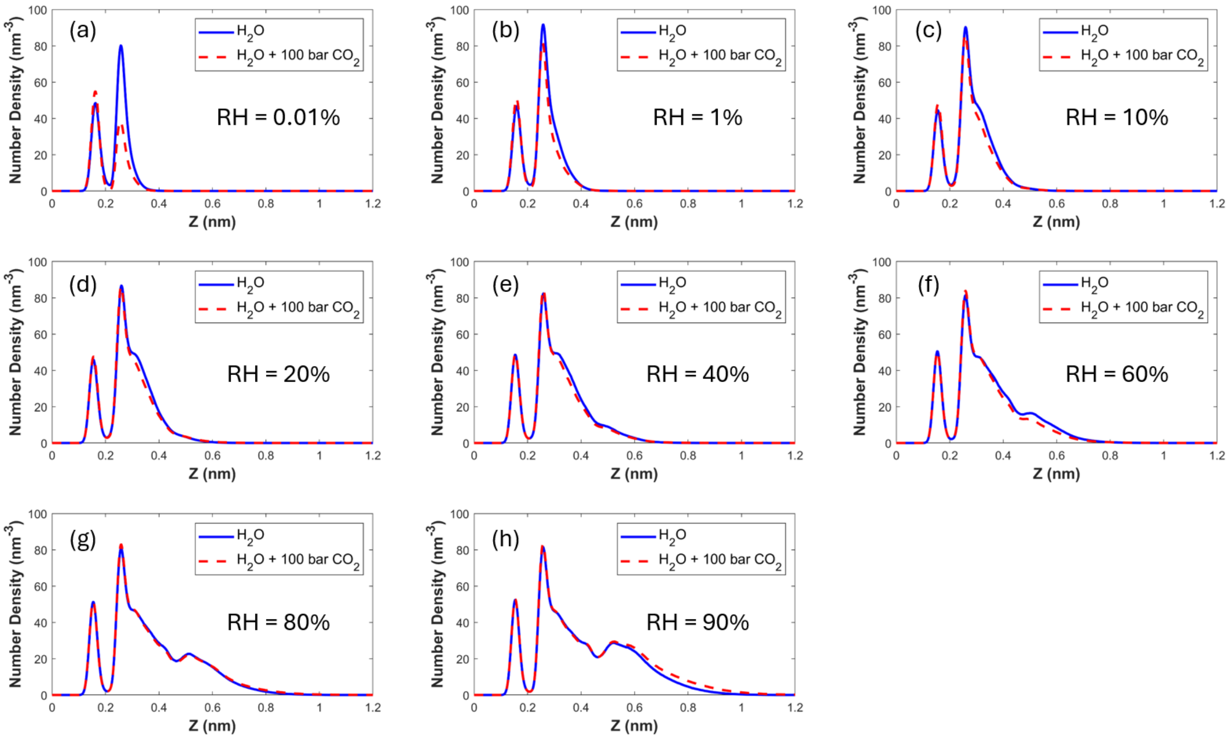

Fig. S1. Comparison of the water density profiles near the lower mica wall when the environmental CO$_2$ pressure is 0 bar and 100 bar at different RHs.

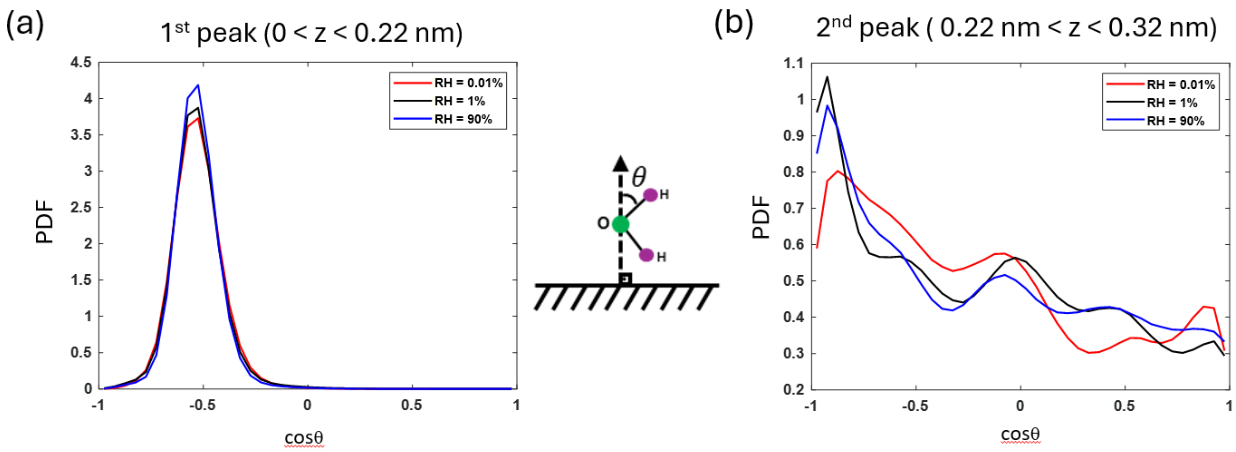

Fig. S2. Orientation distribution of the OH bond of water molecules in the regions $0 < z < 0.22$ nm (i.e., the first water peak at RH = 0.01%) and $0.22 \text{ nm} < z < 0.32$ nm.

To gain a basic understanding of dynamics of water adsorbed on mica, we compute the continuous survival probability (CSP) functions of the water molecules in the first density peak shown in Fig. 9a, as have been done by Malani and Ayappa.[48] In their work, a water slab of about 1.8 nm thick is confined between two mica sheets. CSP(t) measures the probability that water molecules reside continuously in the first density peak between 0 and time *t*. Figure S2a shows that the CSP of water molecules in the first density peak in these systems are essentially the same despite our water film is exposed to vapor but the water in Ref. 48 is confined between mica sheets. Such similarity may be attributed to the fact that water molecules in this peak occupy the ditrigonal cavities and form an ordered lattice on the mica surface,[32] and therefore their dynamics are governed by their interactions with mica. Malani and Ayappa showed that the CSP curve in Fig. S2a corresponds to a residence lifetime of about 15 ps, which is about 10 times larger than that for water molecules in bulk layers of a similar width with the first density peak. The sluggish dynamics revealed here suggest that the first water layer behave more like a solid rather than a liquid.

We also evaluated the dipole orientational correlation function ($C_{\mu,1}$) of the water molecules in the first density peak. As in Ref. 48, $C_{\mu,1}$ is defined as

$$C_{\mu,1}(t) = \frac{1}{\mathrm{CSP(t)}} \frac{\langle \sum_{i=1}^{N} P_1\big(\boldsymbol{\mu}_i(t) \cdot \boldsymbol{\mu}_i(0)\big) \cdot \prod_{t'=0}^{t} \Theta_i(t') \rangle}{\langle \sum_{i=1}^{N} P_1\big(\boldsymbol{\mu}_i(0) \cdot \boldsymbol{\mu}_i(0)\big) \cdot \Theta_i(0) \rangle}$$

where P_1 is the Legendre polynomial of rank 1, $\boldsymbol{\mu}_i(t)$ is the dipole vector of a water molecule *i*, and N is the number of water molecules. The function Θ_i is 1 if a water molecule *i* resides in the first density peak at time *t* and is otherwise *0*. Fig. S2b shows that $C_{\mu,1}$ of the water molecules in the first density peak decays at a time scale larger than 10 ps, similar to that reported in Ref. 48. The slow decay of $C_{\mu,1}$ further supports the sluggish dynamics of water molecules in the first density peak.

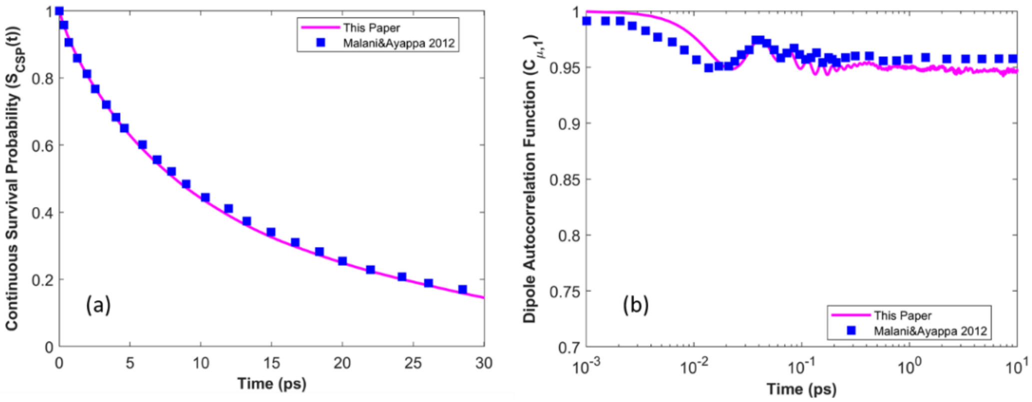

Fig. S3. A comparison of the continuous survival probability function (a) and the dipole orientational autocorrelation function (b) for water molecules in the first density peak near the mica surface obtained in this study and by Malani and Ayappa.[48] In Malania and Ayappa‘s work, water is confined between two mica sheets. In our data shown here, the RH of the water vapor above the mica is 0.01%.

Appendix III - Selection of representative position for water molecules directly exposed to vapor

In the main text, the orientation and interaction energy of the water molecules directly exposed to vapor were analyzed. These molecules are selected to fall into a 0.04 nm-wide bin centering on the position where the mean water density is 5.65 nm^{-3}. The density of 5.65 nm^{-3} was selected based on the position of the third interfacial water layer (i.e., the water layer directly exposed to the vapor phase) at RH = 90%.

Specifically, using the ITIM analysis, we identified three layers of water molecules on the mica surface. For water molecules in each layer, we built a histogram based on their oxygen atoms' z-position, from which the probability density distribution was computed. Figure R3 shows that the probability density peaks at about $z = 0.77$ nm (marked by a black arrow), where the 1D water density profile gives a value of 5.65 nm^{-3}. Therefore, it is reasonable to use water molecules at the location where the 1D density is 5.65 nm^{-3} to present the water directly exposed to the vapor phase.

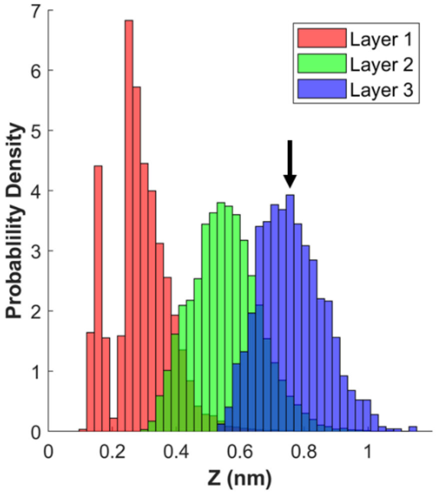

Fig. S4. The probability density distribution of the *z*-position of molecules in the three interfacial water layers on a mica surface at RH = 90%. To compute these distributions, for each saved trajectory frame, we first identify molecules belonging to the first, second, and third interfacial layers as discussed in the main text. Then, for water molecules in each of these layers, we build a histogram based on their oxygen atoms' z-position, from which the probability density distribution is computed.

Appendix IV - Interaction energy of water molecules near the water-vapor interface

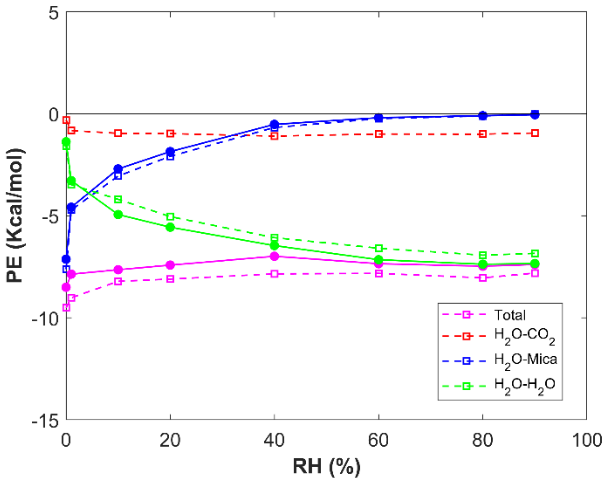

Fig. S5. The average interaction energy of water molecules located at the position where the water density is 5.65 nm^{-3}. Solid (dashed) lines are for situations with a CO_2 pressure of 0 bar (100 bar).